Amplification of Australian heatwaves via local land-atmosphere coupling

Annette L. Hirsch[1,2], Jason P. Evans[1,2], Giovanni Di Virgillio[2], Sarah E. Perkins-Kirkpatrick[1,2], Daniel Argüeso[3], Andrew J. Pitman[1,2], Claire C. Carouge[1], Jatin Kala[4], Julia Andrys[4], Paola Petrelli[5], and Burkhardt Rockel[6]

[1] ARC Centre of Excellence for Climate Extremes, University of New South Wales, Sydney, Australia

[2] Climate Change Research Centre, University of New South Wales, Sydney, Australia

[3] Department of Physics, University of the Balearic Islands, Spain

[4] Environmental and Conservation Sciences, Murdoch University, Perth, Australia

[5] ARC Centre of Excellence for Climate Extremes, University of Tasmania, Hobart, Australia

[6] Institute of Coastal Research, Helmholtz-Zentrum Geesthacht, Geesthacht, Germany

Corresponding Author: Annette L. Hirsch (a.hirsch@unsw.edu.au)

Key Points

1. Spatial variability in the land-atmosphere coupling defines local heatwave sensitivity to antecedent land surface conditions
2. Land-driven coupling regions experience a higher heatwave day frequency with temperatures sensitive to prior soil moisture conditions
3. Antecedent soil moisture anomaly rather than drying rate two weeks prior to a heatwave has a longer impact on heatwave temperatures

Keywords

CORDEX, land-atmosphere interactions, excess heat factor, two-legged coupling

Abstract

Antecedent land surface conditions play a role in the amplification of temperature anomalies experienced during heatwaves by modifying the local partitioning of available energy between sensible and latent heating. Most existing analyses of heatwave amplification from soil moisture anomalies have focused on exceptionally rare events and consider seasonal scale timescales. However, it is not known how much the daily evolution of land surface conditions, both before and during a heatwave, contributes to the intensity and frequency of these extremes. We examine how the daily evolution of land surface conditions preceding a heatwave event contributes to heatwave intensity. We also diagnose why the land surface contribution to Australian heatwaves is not homogeneous due to spatio-temporal variations in land-atmosphere coupling. We identify two coupling regimes: a land-driven regime where surface temperatures are sensitive to local variations in sensible heating and an atmospheric-driven regime where this is not the case. Northern Australia is consistently strongly coupled, where antecedent soil moisture conditions can influence temperature anomalies up to the fourth day of a heatwave. For southern Australia, heatwave temperature anomalies are not influenced by antecedent soil moisture conditions due to an atmospheric-driven coupling regime. Therefore, antecedent land surface conditions have a role in increasing the temperature anomalies experienced during a heatwave only over regions with strong land-driven coupling. The timescales over which antecedent land surface conditions contribute to Australian heatwaves also vary regionally. Overall, the spatio-temporal variations of land-atmosphere interactions help determine where and when antecedent land surface conditions contribute to Australian heat extremes.

Plain Language Summary

Research focused on the Northern Hemisphere has demonstrated that unusually dry soils preceding a heatwave event amplify the hot conditions experienced. However, we don't know whether the daily evolution of how the land surface dries out can amplify heatwave temperatures, or whether any impact is similar across a large area like Australia. In exploring these knowledge gaps, we find that regions where there is a larger drying trend tend to be more sensitive to land water availability and have more heatwave days. We find that the effect of dry soils before a heatwave varies considerably across Australia. Identifying where dry soils have a large impact on heatwaves required classifying the land into regions where soil water variability affects surface temperatures and where it doesn't. This could be extended to other atmospheric processes to differentiate between local and remote influences.

1. Introduction

Climate change is likely to increase the frequency, intensity and duration of heatwaves, particularly over Australia [*Cowan et al.* 2014; *Lewis and King* 2015; *Perkins* 2015; *Perkins and Gibson* 2015; *Horton et al.* 2016]. Heatwaves pose a significant risk to ecosystem function and human health as evident from the impacts of several well-documented case studies including the 2003 European heatwave [e.g. *Fischer et al.* 2007b; *Miralles et al.* 2014], the 2010 Russian heatwave [e.g. *Hauser et al.* 2016] and the 2012/2013 angry summer in Australia [*Lewis and Karoly* 2013; *Perkins et al.* 2014a; *Lewis and King* 2015]. Heatwaves are generally associated with clear skies, increased subsidence, warm air advection and prolonged hot conditions arising from persistent quasi-stationary high-pressure systems [*Miralles et al.* 2014; *Parker et al.* 2014a,b; *Quinting et al.* 2018; *Risbey et al.* 2018]. Over Australia, the synoptic mechanisms that enable blocking highs to persist are generally more transient (~ 1 week) than their European counterparts (~ weeks) [*Risbey et al.* 2018], however, the presence of a blocking high pressure system does not necessarily lead to a heatwave event.

Land surface conditions can amplify surface temperatures, particularly during heatwave events [*Fischer et al.* 2007a,b; *Lorenz et al.* 2010; *Miralles et al.* 2014; *Herold et al.* 2016; *Hauser et al.* 2016; *Gibson et al.* 2017]. Globally, this influence has been attributed to precipitation deficits enhancing negative soil moisture anomalies, facilitating further surface warming by partitioning more energy into sensible heating [*Mueller and Seneviratne* 2012]. Recent amplification of hot temperature extremes associated with anthropogenic climate change is also consistent with changes in the surface energy balance coincident with drying soils [*Donat et al.* 2017]. Projected changes in hot temperature extremes also indicate that the role of soil moisture conditions through land-atmosphere interactions is important [*Vogel et al.* 2017; *Seneviratne et al.* 2013]. In particular, the direct effects of soil moisture on the surface energy balance are necessary for the projected amplified response of regional temperature extremes relative to mean temperature changes [*Vogel et al.* 2017].

The land surface contribution to surface temperatures is not limited to single-day extreme temperature events with several studies demonstrating the role of land surface drying both prior to and during a heatwave event [*Fischer et al.* 2007a,b; *Lorenz et al.* 2010; *Miralles et al.* 2014; *Hauser et al.* 2016; *Herold et al.* 2016; *Gibson et al.* 2017]. For example, *Fischer et al.* [2007a] demonstrated that the presence of land-atmosphere interactions typically increases the number of heatwave days per summer season by 50-80% in Europe. Further work by *Fischer et al.* [2007b] demonstrated that the dry spring preceding the 2003 European heatwave was a necessary condition for this event, in addition to a persistent atmospheric high-pressure system that lasted several months [*Ferranti and Viterbo,* 2006]. This result is corroborated by subsequent studies [e.g. *Lorenz et al.* 2010; *Miralles et al.* 2014]. Other examples include the 2010 Russian Heatwave, where impacts were compounded due to a severe drought [*Flach et al.* 2018]. The land surface drying that occurred prior to the drought increased the likelihood of exceptional temperature anomalies experienced during this event by sixfold [*Hauser et al.* 2016]. Studies focusing on less extreme heatwaves over Europe [*Lorenz et al.* 2010; *Miralles et al.* 2014], North America [*Ford and Schoof* 2016; *Teng et al.* 2016; *Cowan et al.* 2017] and Australia [*Perkins et al.* 2015; *Herold et al.* 2016; *Gibson et al.* 2017] all suggest that, in general, antecedent soil moisture conditions had a role in both the heatwave intensity and to a lesser extent also the duration. This is understandable given these are regions where the atmosphere is sensitive to land surface variability (i.e. the land-atmosphere coupling) [e.g. *Seneviratne et al.* 2013; *Hirsch et al.* 2014; *Lorenz et al.* 2015].

When diagnosing the role of land surface conditions on extreme events such as heatwaves, resolution becomes important for resolving the spatio-temporal variability of land-atmosphere interactions [e.g. *Holgate et al.* 2019; *van der Linden, Haarsma and van der Schrier* 2019]. This is one of the motivations for initiatives such as the COordinated Regional climate Downscaling EXperiment (CORDEX) [*Giorgi et al.* 2009]. Several examples exist that demonstrate the added value of using regional climate models (RCMs) for understanding extremes [*Fischer et al.* 2007a; *Lorenz et al.* 2010; *Salathé et al.* 2010; *Gao et al.* 2012; *Evans et al.* 2014; *Perkins et al.* 2014b; *Andrys et al.* 2015; *Argüeso et al.* 2015; *Hirsch et al.* 2015; *Kala et al.* 2015a; *Di Luca et al.* 2016; *Evans et al.* 2017; *Knist et al.* 2017; *Herold et al.* 2018]. CORDEX simulations provide reasonable high resolution and the internally consistent climate variables required to examine how land-atmosphere feedbacks contribute to the characteristics of heatwaves. CORDEX also provides results from several RCMs and configurations of the same RCM which helps provide improved confidence in the robustness of conclusions in comparison with using a single model [*Perkins and Fischer* 2013].

In an analysis of Australian heatwaves, *Perkins et al.* [2015] contrasted the contribution of soil moisture conditions in comparison with large-scale modes of climate variability. They found that the contribution of antecedent soil moisture at seasonal timescales was not as great as previously demonstrated over Europe. *Kala et al.* [2015a] were able to demonstrate that for the 2009 Victorian heatwave (prior to the Black Saturday bushfires) the contribution of antecedent soil moisture conditions could only be detected at significantly shorter timescales of the order of a week compared to months over Europe. This is likely due to several basic differences between Australian and European conditions. First, Australia is generally drier [e.g. *Nicolai-Shaw et al.* 2017] which is important as antecedent soil moisture conditions on monthly timescales influences the number of heatwave days and the temperatures reached during heatwaves [*Herold et al.*, 2016]. Secondy, the synoptic-scale dynamical settings differ strongly [see *Risbey et al.* 2018] for heatwaves. *Gibson et al.* [2017], for example, examined the role of warm air advection in accelerating the drying of the land surface and demonstrated how local partitioning of the surface energy balance influenced heatwaves under favorable synoptic conditions.

It is therefore clear from the existing literature that the land surface state has an impact on heatwave conditions, both in Australia and elsewhere. However, it is less clear why there are spatial variations in how important this contribution is and how the daily evolution of prior land surface conditions contributes to heatwave intensity. This study examines where and how the land surface contributes to heatwaves in space and time using observations, reanalysis, and the CORDEX RCM ensemble. We also examine how the rate of land surface drying influences the amplitude of temperature anomalies experienced during a heatwave. By examining both observational and model datasets, we gauge the suitablity of the CORDEX AustralAsia ensemble simulations for evaluating the temporal dynamics of land-atmosphere interactions prior and during heatwave events with a focus on the Australian region. This is the first time the CORDEX AustralAsia ensemble has been used to examine heatwave attributes.

2. Methods

2.1 Model Domain and Experimental Design

In this study three RCMs are evaluated including four different physics combinations of the Weather Research and Forecasting Model (WRF) [*Skamarock et al.* 2008], the COnsortium for Small-scale MOdelling model in climate mode (CCLM) [*Rockel et al.* 2008], and the Conformal-Cubic Atmospheric Model (CCAM) [*McGregor and Dix* 2008]. Details on the physics employed in these RCMs are summarized in Table 1. Prior analysis [*Evans et al.* 2012; *Evans et al.* 2014; *Ji et al.* 2014; *Kala et al.* 2015b] was instrumental in determining the four WRF configurations used. The domain (Figure 1) is resolved using a resolution of approximately 50 km (0.44˚ x 0.44˚ on a rotated coordinate system). All RCM data was interpolated using a nearest-neighbor approach from the native resolution of the model to a regular 0.5˚ latitude x 0.5˚ longitude grid to enable direct comparison. As there are almost no changes in the resolution, the nearest-neighbor approach is preferred to other interpolation methods to preserve the extremes at the cost of some location error (up to half a grid cell). All RCMs were driven by ERA-Interim boundary conditions from January 1981 to January 2010.

2.2 Observational and Re-Analysis Datasets

The different RCMs were evaluated using several gridded observational datasets. This includes the Australian Gridded Climate Data (AGCD) daily precipitation and temperature dataset [*Jones et al.* 2009] which was used as the benchmark to which all other data are compared in the identification of heatwave days and their climatological attributes. Although not *in situ* station data, the AGCD dataset closely tracks the station observations with the exception of central western Australia where the network density is sparse [*King et al.* 2013]. The Global Land surface Evaporation: the Amsterdam Methodology (GLEAM) dataset [*Miralles et al.* 2011; *Martens et al.* 2017] is used to evaluate the daily latent heat flux trend prior to all heatwave events. Additional datasets used to evaluate the surface energy fluxes of the RCMs include two reanalysis products: the ERA-Interim (ERAINT) dataset produced by the European Centre for Medium-Range Weather Forecasts (ECMWF) [*Dee et al.* 2011] and the Modern-Era Retrospective Analysis for Research and Applications version 2 (MERRA2) [*Reichle et al.* 2017]. Note that although ERA-Interim is used as the RCM boundary conditions, we include it here: (1) to evaluate the added value gained by using an RCM, (2) to provide a broader classification of the observational uncertainty, and (3) because surface fluxes are not directly used to run the RCMs. A summary of the key references, variables and native resolution of these datasets are provided in Table 2. All datasets were interpolated to the resolution of the RCMs using a conservative remapping algorithm to enable comparison.

2.3 Heatwave Definition and Summary Attributes

There are several ways of defining and identifying heatwaves [e.g. *Perkins and Alexander* 2013; *Perkins* 2015]. Here we use a modified version of the Excess Heat Factor (EHF) originally defined by *Nairn and Fawcett* [2013] that implicitly incorporates a seasonal cycle to characterize heatwaves according to the climatological conditions for a particular time of the year [*Perkins and Alexander* 2013]. Heatwave days are identified by calculating the anomaly in the daily mean temperature (determined from the average of the daily maximum and minimum temperature) using the calendar day 90th percentile determined using all years 1981-2010 (Equation 1). When this anomaly is positive for at least three consecutive days, these are classified as heatwave days. This is iterated for all years and grid points of the respective datasets.

$$EHF_{SIG} = \frac{1}{3}(T_1 + T_{t-1} + T_{t-2}) - T_{90} \quad (1)$$

Here T_{90} corresponds to the spatially explicit (i.e. at each grid cell) 90th percentile of the daily mean temperature corresponding to the calendar day with a temperature T_1. T_{90} is calculated using a 15-day window for all years to provide a sample of 450 (15 x 30) daily values per grid point in estimating the percentile. By using a calendar day estimate of the 90th percentile it is possible to identify heatwaves and warm spells throughout the whole year and not just the hottest months of the year. However, we limit our analysis to heatwaves that occur during the Australian heatwave season defined as November to March (i.e. from the end of the Austral spring to the start of autumn) [*Perkins and Alexander* 2013]. This is also when the soil moisture limitation on evapotranspiration is greatest and therefore the atmospheric sensitivity to land surface conditions, i.e. the coupling strength between the land and the atmosphere, is greatest [*Hirsch et al.* 2014; *Lorenz et al.* 2015]. Once the heatwave days are identified using Equation 1, different attributes of these heat extremes are calculated for each year (Table 3) to describe the amplitude, duration and number of events per year.

2.4 Land Atmosphere Coupling Metrics

Several metrics exist for evaluating land-atmosphere coupling [e.g. *Lorenz et al.* 2015; *Santanello et al.* 2018]. Land-atmosphere coupling here refers to the atmospheric sensitivity to land surface variability. We use the metrics of *Dirmeyer* [2011] and *Dirmeyer et al.* [2013a, 2013b and 2014] to evaluate local land-atmosphere coupling which splits the full land-atmosphere coupling into a terrestrial component and an atmospheric component. It is also possible to interrogate both the hydrological and thermal pathways of the land-atmosphere coupling. Here, we follow the thermal pathway of land-atmosphere coupling that evaluates the covariance of soil moisture (mrso), sensible heat flux (hfss) and 2m air temperature (tas). This includes the terrestrial component:

$$I_L = \sigma_{mrso} \times \frac{d\,hfss}{d\,mrso} = \frac{COV(mrso,hfss)}{\sigma_{mrso}} = \frac{\sum(mrso-\overline{mrso})(hfss-\overline{hfss})}{\sqrt{\frac{1}{N}\sum(mrso-\overline{mrso})^2}} \quad (2)$$

The atmospheric component:

$$I_A = \sigma_{hfss} \times \frac{d\,tas}{d\,hfss} = \frac{COV(hfss,tas)}{\sigma_{hfss}} = \frac{\sum(hfss-\overline{hfss})(tas-\overline{tas})}{\sqrt{\frac{1}{N}\sum(hfss-\overline{hfss})^2}} \quad (3)$$

Finally, the whole coupling pathway:

$$I_{LA} = \sigma_{mrso} \times \frac{d\,tas}{d\,mrso} = \frac{COV(mrso,tas)}{\sigma_{mrso}} = \frac{\sum(mrso-\overline{mrso})(tas-\overline{tas})}{\sqrt{\frac{1}{N}\sum(mrso-\overline{mrso})^2}} \quad (4)$$

Where σ_X denotes the standard deviation of variable X, dY/dX the slope of the linear regression of Y on X, COV(X,Y) the covariance between X and Y, N the number of values and $\bar{X}$ is the average of variable X. All metrics are calculated using standardized daily anomalies of the variables following *Dirmeyer* [2011]. Each component and the whole coupling pathway is evaluated at each grid cell, to characterize the local land-atmosphere coupling and for each heatwave season to account for interannual variability in the coupling diagnostics. By construction, the σ_X term in these coupling metrics means that where the land surface variability is negligible, the land-atmosphere coupling is weak. To enable comparison between the coupling diagnostics, we normalise them according to:

$$Z = \frac{I_x - \mu}{\sigma} \tag{5}$$

Where μ and σ denote the spatial mean and standard deviation, respectively. This converts the units of all coupling indices to a non-dimensional value. We use a threshold of ±0.1 to denote weak coupling unless stated otherwise. An evaluation of the potential role of non-local coupling is the focus of a subsequent study. These metrics have previously been used over Australia to characterize land-atmosphere coupling and to distinguish between different coupling regimes [*Hirsch et al.* 2016].

2.5 Likelihood Ratio

To evaluate whether differences in the land-atmosphere coupling can explain spatial differences in the land surface contribution to heatwaves we use the likelihood ratio (LR) metric of *Stott et al.* [2004]. We calculate the 90th percentile across all heatwave events that occurred within a region of interest for each EHF_{SIG} diagnostic. Then we use the 90th percentile as a threshold to calculate the probability of exceeding this value for regions where the land-atmosphere coupling is considered a land-driven regime. We also separately calculate the probability over regions that are considered an atmospheric-driven regime, i.e. where the surface temperatures are driven by atmospheric variability:

$$LR = \frac{Pr(Extreme\ Heatwave\ |\ I_A > 0.1)}{Pr(Extreme\ Heatwave\ |\ I_A < -0.1)} \tag{6}$$

This diagnostic is evaluated using all grid cells (and therefore not spatially explicit) and all heatwave years for each dataset independently unless otherwise specified.

3. Results

3.1 Model Evaluation

In this section we evaluate how well the RCMs simulate the climatological attributes of Australian heatwaves in the context of observational uncertainty. We also examine the temporal evolution of the surface energy balance for the 30 days prior to a heatwave event.

A critical component for the identification of the heatwave days is the threshold (T_{90} in Equation 1) to which the EHF_{SIG} indices are determined. Figure 2 illustrates the annual mean value of this threshold for AGCD with the bias between the reanalysis datasets and each respective RCM simulation. For the RCMs, biases that are within the observational uncertainty are masked in white. In general, MERRA2 has a T_{90} value that is 1-2˚C warmer than that of AGCD (Figure 2b) and ERAINT is almost always within ±1˚C of AGCD (Figure 2c). Regarding the RCMs, WRFJ, WRFK and WRFL all have a cool bias in T_{90} ranging from 2-4˚C (Figure 2d-f) with the largest cold biases (locally >4˚C) from the WRFL model (Figure 2f). The other three RCMs, WRFM, CCLM and CCAM, have a warm bias of up to 3˚C. *Di Virgilio et al.* [2019] found biases in the temperature distributions in all of these RCMs and the T_{90} biases (Figure 2) are reflective of this result.

The biases in the threshold used to define heatwave days propagate through all the heatwave diagnostics presented in this study (Figure 3) as it affects the frequency to which heatwave days are determined. The skill of each RCM in capturing the climatological heatwave attributes is summarized in Figure 3 with the individual contour maps for the amplitude and frequency provided in the supplementary material (Figures S1 and S2 respectively). The left-hand side of Figure 3 denotes the observational uncertainty between AGCD, MERRA2 and ERAINT. This is constructed by evaluating the 10^{th} and 90^{th} percentile range of the spatial differences between each of the observational datasets for each EHF diagnostic. The right-hand side of Figure 3 denotes for each model how much the model bias exceeds the observational uncertainty. This has been constructed by evaluating the 10^{th} and 90^{th} percentiles of the spatial model bias and comparing this to the 10^{th} and 90^{th} percentile range of the observational datasets. More specifically, if the 90^{th} percentile of the model bias exceeds the 90^{th} percentile of the observational range, the model bias is coloured red. Similarly, if the 10^{th} percentile of the model bias is less that the 10^{th} percentile of the observational range, the model bias is coloured blue. We consider the 10^{th} and 90^{th} percentiles to avoid the effects of cancellation when the spatial biases are both negative and positive. All values in Figure 3 are converted to percentages using the AGCD data for consistency with Figures 2, S1 and S2 to enable comparison between the EHF_{SIG} diagnostics. In general, most of the WRF models tend to under-predict the temperature amplitude relative to AGCD (HWAt and HWMt) during heatwaves while the remaining RCMs are too warm. All models tend to under-predict the frequency of heatwave days (HWF) which is subsequently reflected in the number (HWN) and duration (HWD and HWL) of events. All biases are however within 10% of the observational uncertainty. While bias correction methods could be applied to the temperature data, this would prohibit any analysis of the physical mechanisms, particularly those corresponding to land-atmosphere interactions [*Maraun et al.* 2017].

To examine the RCM skill in simulating the temporal evolution of the land surface leading in to a heatwave we examine anomaly time series (Figure 4) for a subset of climate variables and spatially aggregated over the sub-regions depicted in Figure 1. An extended version of this figure is available in the supplementary material (Figure S3). The sub-regions have been selected according to previous research by *Gibson et al.* [2017] where heat advection during a heatwave is substantial with two additional regions that have predominantly distinct land-atmosphere coupling regimes (discussed later). There is a coherent time evolution across all models and reanalysis with AGCD for the daily mean 2 m air temperature (tas) (Figure 4 top row). The peak in the temperature anomaly ranges between day 4 and 6 of the event with higher temperature anomalies experienced over the Nullarbor Plain (NP; > 5˚C) compared to the wetter regions of South-East Australia (SEA; 4˚C) and Northern Australia (NA; 3˚C). The corresponding anomaly time series for precipitation (pr) (Figure 4 second row) indicates a regional dependence linked with the precipitation regime of the respective region. For example, NA shows a considerable decrease in precipitation with large negative precipitation anomalies prior to a heatwave, with considerable spread between models. The precipitation regime is monsoonal over NA, where RCM biases evaluated by *Di Virgilio et al.* [2019] indicate that all RCMs except WRFM tend to underestimate the magnitude of the precipitation anomaly. For SEA and NP, the precipitation anomaly time series are more coherent across the datasets. For NP, the smaller anomalies are indicative of the low annual rainfall that this region experiences. During a heatwave event, the negative precipitation anomalies are expected because of the conditions required to reach very hot temperatures. Note that in all regions the precipitation anomalies return to zero from day 6 of the heatwave. The soil moisture (mrso) anomaly time series (RCMs only) closely reflect the changes in the precipitation anomaly time series (Figure 4 third row). Here, the regional dependence of any land surface contribution is evident. In particular, NA shows the largest trends in the soil moisture, indicative of the wetter conditions in this region compared to NP where soils are extremely dry with limited change both before and after a heatwave. Finally, the latent heat flux (hfls) anomaly time series (Figure 4 bottom row) show similar trends to the soil moisture anomaly time series and reflect how the land surface drying contributes to more energy being partitioned into sensible heating (see supplementary material) and likely contributing to the larger temperature anomalies during heatwave events. The regional contrast also extends to the sensible heat flux (Figure S3 fifth row) where drier locations (e.g. SA, NP, SWA) show a decreasing trend during the heatwave event consistent with the advection of a warm air mass over the region. This was confirmed when examining the low-level heat advection (not shown). The anomaly time series of both the downward short- and longwave radiation (Figure S3 rows six and seven respectively) show opposite tendencies during the heatwave event across the sub regions. More specifically, for wetter regions (e.g. NA, EA, SEA) there are smaller anomalies in the downward longwave radiation (~5 W m^{-2}) and larger anomalies for the downward shortwave radiation (10 – 40 m^{-2}). In contrast, for drier locations (e.g. SA, NP and SWA) the opposite occurs. This suggests that the classification of heatwaves could be split into wet and dry events. In the wetter regions, there is a clear drying trend ahead of the event (Figure 4 and S3, rows 2 and 3) with a corresponding shift in the Bowen ratio towards greater sensible heating. The increase in downward shortwave radiation (Figure S3 row seven) is consistent with a decrease in cloud cover. Conversely, in the drier regions, the only large anomaly is in the downward longwave radiation, which increases ahead and during the event, with smaller and even negative changes in downward shortwave radiation. The latter suggests that events over these regions are less likely to correspond to clear sky conditions with the changes in sensible heating noted earlier indicating the events over these regions are dominated by heat advection. Finally, there is considerable spread between the RCMs and reanalysis data for all variables except temperature. Note that CCLM and CCAM have larger positive anomalies in downward shortwave radiation compared to the other RCMs (Figure S3) which may contribute to the warmer biases in Figures 2 and 3.

Given the negative anomaly trend in latent heating, Figure 5 shows the probability of land surface drying, defined according to the latent heat flux trend, over the two-week period prior to a heatwave event. This is calculated from the trend in the two-week anomaly time series for each heatwave event over 1980-2009, with probabilities less than 0.5 masked in white. For AGCD/GLEAM and MERRA2, the probability ranges from 60-80% indicating that for large areas of Australia land surface drying prior to a heatwave is a frequent phenomenon. Prior land surface drying is not a necessary requirement, as the synoptic conditions favoring the onset of heatwaves will also favor drying soils due to clear skies and high net radiation. However, antecedent land surface conditions may influence the temperatures experienced during a heatwave, which is examined in the following section. For the RCMs the probability of land surface drying is not as high, particularly over the southeast coast of Australia where the proportion is often below 55. There could be several reasons for this that may stem from limitations in resolving the local complex flows arising from the interaction of sea-breezes, changes in elevation associated with the Great Dividing Range or deeply rooted vegetation providing a buffer. Overall, a high probability of surface drying is to be anticipated as the land surface dries out in the absence of precipitation. However, there are occasions where a heatwave is not preceded by a decreasing trend in the latent heat flux. For example, for CCLM (Figure 5h) the probability of a negative latent heat flux trend is below 50% which is consistent with the CCLM time series in Figure 4 for NA. These probabilities are robust where different periods were tested to evaluate the sensitivity of these probabilities (i.e. calculating the 1-week and 3 week pre-heatwave trend and the trend between the last rainfall event and the heatwave start). In the following section we examine whether prior drying of the landscape has any impact on the temperatures experienced during a heatwave.

3.2 Do antecedent land surface conditions influence heatwaves?

From this section onwards, the analyses will focus only on the model results where all variables are available and therefore their co-evolution can be examined comprehensively. We examine whether the distribution of the trend in the latent heat flux anomaly time series is sensitive to antecedent soil moisture conditions. To do so, we split the trend estimates according to the soil moisture anomaly two weeks prior to each heatwave into the driest (Q1 < 25^{th} percentile), the interquartile range (Q1-Q3: between the 25^{th} and 75^{th} percentiles), and the wettest (Q3 > 75^{th} percentile) anomalies. For each group we calculate the kernel density function as a non-parametric estimator of the underlying probability distribution.

Figure 6 shows that the two-week trend in the latent heat flux anomaly time series is sensitive to soil moisture conditions for all sub-regions denoted in Figure 1. A two-sample Kolmogorov-Smirnov test confirms that the distributions of the trend in the latent heat flux anomalies are significantly different (with p-values < 1%) between the wettest and driest antecedent soil moisture conditions. In particular, if soil moisture conditions two-weeks prior to a heatwave are wetter (Q3), then there are larger decreasing trends in the latent heat flux anomaly time series. This is indicative of land surface drying, either through soil drainage or evaporation, that is expected to occur in the absence of precipitation.

We next examine whether the soil moisture state in the two weeks preceding a heatwave contributes to the temperature anomalies experienced on the first day (Figure 7), and then subsequent days (see supplementary material) of a heatwave event using the same methodology as that used to construct Figure 6. In Northern Australia, Eastern Australia and South East Australia the probability of warmer temperature anomalies on the first day of the heatwave is higher when antecedent soil moisture conditions are dry and the difference between the wettest and driest antecedent soil moisture conditions is statistically significant for these regions. This is robust across individual RCMs (e.g. Figure S4 for Northern Australia). However, for South Australia, the Nullarbor Plain and South West Australia, the temperature distributions are not statistically different when split according to the soil moisture state. This is likely due to the dry conditions with limited soil moisture variability as indicated in Figures 4 and 6; shorter periods were tested but did not change the results. Results are similar for the influence of antecedent soil moisture conditions on the second day of the heatwave (Figure S5). Indeed, for Northern Australia, the influence of antecedent soil moisture conditions is evident up to day four of the heatwave (Figure S6). The contrast between Northern Australia and the other regions can be attributed to greater variability in land water availability linked to the strength of monsoon activity. Therefore, the influence of prior land surface drying on amplifying temperature anomalies experienced during a heatwave is regionally dependent, a result consistent with previous analysis over Australia [*Herold et al.* 2016].

The anomaly time series analysis (Figure 4) reveals that some, but not all, regions have a decreasing trend in the latent heat flux over the 2-weeks prior to heatwave events, we also examine whether the sign of the trend has an impact on the heatwave temperature anomalies (Figure 8). Most regions indicate that the sign of the trend can have a marginal impact on the first day of a heatwave event although the probability of warmer temperatures on the first heatwave day is slightly higher if there is a decreasing trend leading into the event. The effect appears to be short-lived compared to the impact of the antecedent soil moisture anomaly, where the subsequent heatwave days show no sensitivity to the latent heat trend (see discussion in Section 4.1).

3.3 Characterization of local land-atmosphere coupling

To understand if regional differences in the contribution of antecedent soil moisture conditions on temperature anomalies (experienced during a heatwave) exist, we examine the different land-atmosphere coupling metrics described in the methods section. All indices have been normalized such that values exceeding ±0.1 are considered strong. The terrestrial coupling component (Equation 2; Figure S7) confirms that the coupling between soil moisture and the turbulent surface energy fluxes is strong for most of the continent, consistent with Figure 6. Note that the negative values for this coupling metric are indicative of the inverse relationship between soil moisture and sensible heat. For the atmospheric coupling component (Equation 3; Figure 9) it appears that there are two regimes. The first considers regions where I_A is negative, which we classify as the 'atmospheric-driven regime'. The sensible heat flux is a function of the gradient between the surface air temperature (T_a) and the skin temperature (T_s) and therefore when I_A is negative this indicates that changes in Ta are driving the variations in the sensible heat flux. The second considers regions where I_A is positive, which we classify as 'land-driven regime'. Here, changes in surface air temperature are influenced by the soil moisture limited variations in the sensible heat flux. For all models, land-driven coupling ($I_A > 0.1$) is predominantly concentrated over Northern Australia, extending southward along inland eastern Australia and parts of South-west Western Australia. Indeed, the atmospheric coupling (I_A) estimates for all but CCAM show a strong resemblance to the regions of strong land-driven coupling identified by *Hirsch et al.* [2014] which used a different coupling metric. Regions where surface temperature is driven by atmospheric variability coincide with the east coast, Nullarbor Plain, western Australia and Tasmania in all models except for CCAM (Figure 9f). Note that the sub-regions of Eastern Australia, South East Australia, South Australia and South West Australia (denoted in Figure 1) span both coupling regimes. When considering the full land-atmosphere coupling pathway I_{LA} (Equation 4; Figure S8), regions where the land and the atmosphere are strongly coupled differ slightly from those determined using $I_A > 0.1$. Regions where this inconsistency arises include the east coast, Victoria and the Nullarbor Plain. Northern Australia is the one region where all three coupling metrics consistently indicate strong land-driven coupling which may explain why over this region land surface drying can be linked to hotter conditions up to the fourth day of a heatwave event (Figure S6).

3.4 Influence of local land-atmosphere coupling on heatwaves

Given the spatial differences in the atmospheric coupling component I_A (Figure 9), the following analysis determines whether the coupling regime has an influence on the heatwave attributes derived from the EHF_{SIG} (Equation 1). In general, the number of grid cells where there is an atmospheric-driven regime (I_A < -0.1) are lower (30%) than the number where it is a land-driven regime (I_A >0.1; 63%) (Figure S9). This results in different distributions between the coupling regimes for all EHF_{SIG} diagnostics which can distort the calculation of the joint probability distribution. Therefore, examination of the marginal probability distributions is done separately for each coupling regime (land-driven: I_A > 0.1 and atmospheric-driven: I_A < -0.1) in Figure 10. For the heatwave amplitude above the T_{90} threshold per hottest event and on average (HWAt and HWMt), the marginal distributions are clearly distinguishable and statistically different between the coupling regimes (Figure 10a and 10d). Interestingly, the distributions for the atmospheric-driven regions tend to experience hotter conditions than over the land-driven regions where local land-atmosphere coupling is strong. For example, for HWAt, the probability of exceeding 4˚C is twice as likely for the atmospheric-driven regions than for the land-driven regions (LR_{90} = 0.48). It is likely that the contrast between the coupling regimes is sensitive to the background climate conditions. The T_{90} threshold is cooler over the south-eastern coastal regions (Figure 2a) where there is atmospheric-driven coupling (Figure 9) and therefore, when heatwaves do occur there is a lower baseline against which to calculate the anomaly. For the heatwave duration per longest event and on average (HWD: Figure 10b and HWL: Figure 10e), the distributions are insensitive to the coupling regime and the likelihood ratios are close to 1. For the frequency of heatwave days (HWF: Figure 10c) and number of events (HWN: Figure 10f) the differences in the distributions are subtle with a two sample Kolmogorov-Smirnov test confirming that the distributions are statistically different. For example, when HWF > 4 % days there is a higher probability of getting consecutive days exceeding the T_{90} threshold (i.e. EHF_{SIG} > 0) over the land-driven regions where the land-atmosphere coupling is strong (LR_{90} = 1.66). With higher chances of clustering of extreme heat, it is anticipated that this also translates into the number of events. For HWN, this would appear to be the case, where it is twice as likely to get more than 4 heatwave events in a given year over land-driven regions than atmospheric-driven regions (LR_{90} = 2.07). In summary, although heatwaves are triggered less frequently over atmospheric-driven regions where the air temperature is decoupled from local land surface variability, when they do get triggered they are more likely to be more extreme events. For eastern Australia at least, this may also be associated with the lower temperature threshold (T_{90}, Figure 2) where there is potential for stronger anomalies to develop during a heatwave.

Focusing on the sub-regions that span both coupling regimes, Figure 11 suggests that the contrast between coupling regimes has some sensitivity to the soil moisture climatology. Both EA and SEA generally have wetter soil moisture conditions but with higher variability compared to the SA and SWA regions where it is considerably drier with low variability (Figure S10). Given the role that soil moisture conditions have on the partitioning of available energy between sensible and latent heating it is likely that these regional differences in soil moisture, in addition to the local land-atmosphere coupling (i.e. Figure 9), are important for contrasting heatwave statistics between coupling regimes. EA and SEA (Figures 11a, 11b, 11e, and 11f) indicate that where there is strong land-driven coupling there are more consecutive heatwave days with likelihood ratios of 1.75 and 3.09, respectively. However, despite having a higher frequency in heatwave days over the land-driven coupled regions, the probability for very hot events over these regions is smaller compared to atmospheric-driven coupled regions where the likelihood ratios are 0.74 and 0.55 respectively. For SA, the peaks of the mean heatwave amplitude (HWMt) distributions (Figure 10c) differ at 1.2 ˚C for atmospheric-driven regions and 1.8 ˚C for land-driven regions but in the upper tail (HWMt > 2.5 ˚C) there is little distinction between coupling regimes with a likelihood ratio of 1.01. There are also subtle differences in the frequency of heatwave days between coupling regimes for SA (Figure 11g). In particular, for HWF > 4 % days the frequency of clustering of hot days is more likely where there is strong land-driven coupling (LR_{90} > 1.6). SWA is a region where the behavior contrasts from the other three regions. In particular, SWA appears to be the only region where the probability for temperature magnitudes > 2.5 ˚C is 2.41 times more likely when there is strong land-driven coupling than atmospheric-driven coupling (Figure 11d). Furthermore, over SWA the frequency of heatwave days is substantially less probable when there is strong land-driven coupling (LR_{90} = 0.28; Figure 11h). This reversal in behavior between SWA and the other three regions may stem from the very dry soil moisture conditions and limited variability prior to a heatwave event (e.g. Figure S3). Therefore, Figure 11 suggests that the influence of the coupling regimes vary across Australia.

The results in Figure 9 showed that there is considerable variability between the RCMs in the estimation of the local land-atmosphere coupling (I_A). The analyses presented in Figures 10 and 11 show the results from aggregating all RCMs together. Therefore, to illustrate the model dependence we present the national estimates of the likelihood ratio for each EHF_{SIG} diagnostic and RCM (Figure 12). In particular, model dependence cannot be ignored in our analyses. For heatwave amplitude (e.g. HWAt: Figure 12a; HWMt: Figure 10d), the CCAM model shows contrary results to the other models. This contrast may stem from the fact that CCAM has a predominantly strong land-driven coupling regime across Australia (e.g. Figure 9f) and that the temperature distribution was generally warmer relative to the observational datasets to which we evaluate it against (e.g. Figure 2i). However, the WRFM and CCLM also had a warm bias (Figures 2g and 2h) but do not show the same behavior as CCAM as these models had a less skewed distribution of the atmospheric coupling index (I_A; Figures 9d and 9e). All models except CCAM indicate that atmospheric-driven regions tend to have hotter heatwaves when they occur with likelihood ratios of less than 0.6 which collectively mask the behavior of the CCAM model. The heatwave duration (HWD: Figure 12b; HWL: Figure 12e) shows that the model dependence has a greater impact when considering events that are exceptionally long (HWD) rather than in the mean (HWL). In particular, all models suggest that there is limited differentiation between the coupling regimes when it comes to the mean heatwave duration (HWL: Figure 12e) with likelihood ratios within 0.84 to 1.22. However, for the longest heatwave events (Figure 12b) there is a larger spread across the models in the likelihood ratios (0.77 to 1.77) that is masked when aggregating the data across all models in Figure 10b (which had LR_{90} = 1.14). The contrast between HWD and HWL regarding model dependence likely stems from the sample size to which HWD and HWL are estimated from (i.e. HWD has one value per year per grid cell whereas HWL is derived from the average of all events in a given year per grid cell) and therefore HWL is less susceptible to model dependence as it describes average heatwave length.

The percentage of heatwave days (HWF; Figure 12c) and consequently the number of heatwave events (HWN: Figure 12f) also show considerable model uncertainty. In particular, for HWF the likelihood ratio ranges from 1.22 to 5.22, which is not reflected in the all RCM aggregated result of 1.66 in Figure 10c. This uncertainty stems from the larger estimates in WRFM and CCLM which, like CCAM, had warm biases in the temperature distribution. Although all EHF_{SIG} diagnostics for a given model use the corresponding calendar-day estimates of the T_{90} threshold of that model, it would appear that for WRFM and CCLM heatwave days are substantially more likely (~3 and ~5 times respectively) when there is strong land-driven coupling. Given the uncertainty in HWF, it is expected that this also translates into the estimation of the HWN likelihood ratios, with WRFM and CCLM again showing a higher probability of a heatwave event when there is strong land-driven coupling. Therefore, model dependence as demonstrated in the likelihood ratios is linked to both differences in the estimated land-atmosphere coupling strength and the accumulation (and subsequent dissipation) of heat that is likely driven by differences in how various processes are parameterized in the respective models.

4. Discussion

This paper presents the first evaluation of the CORDEX AustralAsia multi-model ensemble in the simulation of various heatwave attributes including how land surface conditions evolve prior to and during a heatwave event. There are four main points that we discuss: (1) the influence of the spatial variability of the land surface on heatwaves; (2) contrasting land contribution from different coupling regimes; (3) model dependence and observational constraints; and (4) comparison to existing literature.

4.1 Influence of the spatial variability of the land surface on heatwaves

The extent to which we diagnose a land surface contribution to the surface temperatures experienced during a heatwave using the CORDEX AustralAsia ensemble is regionally dependent and linked to the land-atmosphere coupling strength of each RCM. Over northern regions with greater land water availability, surface temperatures are sensitive to antecedent soil moisture conditions for longer as latent heating continues to decrease during the event, with corresponding increases in sensible heating indicating a shift in the energy partitioning. In particular, Northern Australia is a region where the land-atmosphere coupling is consistently land-driven for all RCMs, and where antecedent soil moisture conditions can influence temperatures up to the fourth day of a heatwave event. High rainfall variability and the seasonal monsoon increases the land water availability in this region. This contributes to the soil moisture variability and influences the partitioning between sensible and latent heating (Figure 4), consistent with *Hirsch et al.* [2014]. This is confirmed by the variability of the soil moisture (Figure S10) and sensible heat flux (Figure S11) which is used to estimate the land-atmosphere coupling strength. Regions where there is high soil moisture variability coincide with regions where the land-driven coupling ($I_A > 0.1$; Figure 9) was strong. In contrast, for Southern Australia (e.g. the sub-regions of South Australia, Nullarbor

Plain and South West Australia), there is no sensitivity to antecedent soil moisture conditions and there is an absence of strong land-driven coupling (e.g. Figure 9). This is associated with low soil moisture variability (e.g. Figure S10) which limits the potential to perturb the atmosphere. Further, the decrease in sensible heating and increase in downward longwave radiation implies that heatwaves over these regions are dominated by low-level heat advection, which will require further research to confirm. The East Australia and South East Australia regions had moderate sensitivity to antecedent soil moisture conditions, with temperatures on the first and second day of the heatwave event responding to differences in soil moisture. Over these regions, other mechanisms involving adiabatic warming and heat advection have a greater influence on surface temperatures [*Quinting et al.* 2018].

In our analysis, antecedent soil moisture conditions, rather than the latent heat flux trend, had a greater impact on heatwave temperature anomalies. There are several reasons that could explain this result. First, the steepest trends in the latent heat flux were present for Northern Australia (Figure 4). Many regions indicate that dry soil moisture anomalies are a persistent feature during the heatwave season. Therefore, particularly for drier locations, most trends in the latent heat flux are likely not statistically significant for individual time series. Screening to remove data corresponding to where and when trend estimates were close to zero did not change this assessment. Second, across the RCMs and the observations, there was considerable variability in the temporal evolution of land surface conditions. More specifically, some models do not show a strong decreasing trend in the latent heat flux prior to a heatwave event (e.g. Figure 4 for CCLM Northern Australia). However most models do exhibit a decrease in latent heating during a heatwave event but varying from 2 to 7 days in duration. Therefore, it is harder to establish the heatwave temperature sensitivity to short-lived latent heat trends, particularly when they can vary substantially between model and observational estimates relative to the more robust antecedent soil moisture anomaly that is present in all datasets analysed here. This does not rule out that daily changes in the energy partitioning prior to and during a heatwave are not important, just that their contribution is harder to diagnose relative to other features that are more persistent.

It is possible that the spatial variation of the soil hydraulic properties and vegetation types play a role in the spatial variability of the land surface contribution to heatwaves. To diagnose this, we require information on these characteristics that is unavailable for all RCMs. Ideally, we would require RCM outputs for each plant functional type within each grid cell to diagnose the potential role of vegetation characteristics. In the absence of these soil and vegetation properties, our analysis is limited to the role of soil moisture variability. Overall, the results from the CORDEX AustralAsia ensemble, using just the soil moisture information, is consistent with the prevailing theory on how land surface conditions contribute to the amplification of surface temperatures during a heatwave [*Miralles et al.* 2014].

4.2 Contrasting land contribution from different coupling regimes

Our analysis reveals that the contribution of local land surface conditions in the RCMs is spatially inhomogeneous. We characterize two coupling regimes: areas where the atmosphere is sensitive to local land surface variability (land-driven coupling) and regions where the atmosphere is insensitive to local land surface variability (atmospheric-driven coupling). The identification of these two coupling regimes provides a basis to distinguish between where local land surface conditions contribute to heatwaves from where atmospheric mechanisms dominate. Our results demonstrate that the frequency of heatwave days in all RCMs is sensitive to the coupling regime, even when limiting the analysis to regions where the background climate is similar (e.g. Figure 11). All RCMs, except CCAM, suggest that atmospheric-driven regions have a higher likelihood of more extreme conditions when heatwaves occur, indicating that atmospheric mechanisms are the dominant factor contributing to the accumulation of heat.

Although the aggregated RCM results suggest that the coupling regime has no impact on the duration of heatwave events, the impact on the frequency of heatwave days indicates that there may be limitations in how heatwave days are identified using the EHF_{SIG} in individual RCMs. In particular, the possibility that two events are only separated by one day where the EHF_{SIG} is not positive cannot be excluded. To resolve this would require relaxing the condition on consecutive days and could be considered in future research. This may explain why the frequency diagnostics (HWF and HWN) are sensitive to the coupling regime while the duration diagnostics (HWD and HWL) are not, at least when all RCM results are aggregated. For individual RCMs, there is some uncertainty on the role of land-atmosphere coupling for the duration of the longest events (Figure 12b). Generally, our results suggest that identifying the contribution of antecedent soil moisture conditions on heatwaves, particularly the intensity rather than duration, is possible when accounting for where and when the land-atmosphere coupling is land-driven.

4.3 Model Dependence and Observational Constraints

In general, we find that the RCMs can capture the climatological attributes of Australian heatwaves with reasonable skill where biases are within ±10% of the observational uncertainty. Further analysis of the temporal evolution of various climate variables demonstrate that the desiccation of the land surface prior to a heatwave event elevates surface warming via enhanced sensible heating. It is hard to establish how realistic this is in comparison to actual observations. Flux tower observations are too sparse across Australia and records are of insufficient duration to facilitate a full validation of the RCM results. Reanalysis datasets come with their own limitations that contribute to the observational uncertainty [e.g. *Decker et al.* 2012]. The anomaly time series of the latent heat flux in Figure 4 highlights that the uncertainty between GLEAM, MERRA2 and ERAINT is considerable. While several gridded observational products do provide monthly or sub-monthly estimates, our methodology requires daily data to examine the co-evolution of several climate variables both before and during a heatwave event. Remote sensing may provide an opportunity to verify the CORDEX results in the future, but only if daily timescales are resolved.

Given these observational constraints, we acknowledge that our results are subject to model dependence as clearly evident in Figure 12. Our analysis suggests the value of utilizing a multi-model ensemble in identifying the land surface contribution to heatwaves. There are a few caveats to diagnosing the differences between models. This includes differences in how various processes have been parameterized (e.g. convection, radiation, microphysics, land surface) and the impact that this has on the feedbacks and interactions between the schemes. The characterisation of the land surface heterogeneity also determines the instantaneous coupling between the land surface scheme and the atmospheric model. Future research is planned to disentangle which factors provide the largest contributions to the model uncertainty.

4.4 Comparison to Previous Research

Our results are consistent with European studies that suggest that drier antecedent soil moisture conditions are associated with hotter conditions during heatwaves [e.g. *Fischer et al.* 2007a; *Lorenz et al.* 2010; *Miralles et al.* 2014; *Hauser et al.* 2016]. Both *Fischer et al.* [2007a] and *Lorenz et al.* [2010] show that land-atmosphere interactions are important for the persistence of heatwave days, which we also find in our results, particularly over regions where the local land-atmosphere coupling is strongly land-driven (i.e. higher frequency of heatwave days: HWF).

Similar links between the spatial variability in the land surface contribution to heatwaves and the coupling regimes that we identify over Australia have been found for Europe. *Fischer et al.* [2007a] demonstrate that the effect of land-atmosphere coupling is strongest over continental areas and weakest over coastal zones, with corresponding differences in the number of heatwave days. *Knist et al.* [2017] also evaluate land-atmosphere coupling in the EURO-CORDEX simulations and found that the strength of the land-atmosphere coupling is a model dependent quantity with strong land-driven coupling identified over Southern Europe (compared to the cooler energy-limited Northern Europe). *Knist et al.* [2017] conclude that the multi-model estimate provides a good approximation of the observed land-atmosphere coupling. Nevertheless, the areas in our study that were identified across all models as strongly land-driven tend to agree with observationally derived estimates [e.g. *Seneviratne et al.* 2010] and previous model estimates over Australia that used different metrics to those used in this paper [e.g. *Hirsch et al.* 2014; *Lorenz et al.* 2015; *Decker et al.* 2015]. While beyond the scope of this paper, the approach by *Fischer et al.* [2007a] and *Lorenz et al.* [2010] involves prescribing soil moisture conditions could help demonstrate the importance of land-atmosphere interactions for Australian heatwaves, particularly in terms of quantifying the temperature amplification and frequency of heatwave days.

The examination of antecedent soil moisture on European heatwaves has often focused on exceptional events where the preceding spring soil moisture was important [e.g. *Fischer et al.* 2007b; *Miralles et al.* 2014; *Hauser et al.* 2016]. Research on Australian heatwaves demonstrates some uncertainty on what timescale is most appropriate to diagnose a land surface contribution. *Kala et al.* [2015a] focused on a single event and examined the sensitivity to soil moisture conditions 15 days prior to that event. In contrast, *Herold et al.* [2016] used a 3-month time scale when examining the potential role of antecedent soil moisture conditions on heatwaves. Finally, *Perkins et al.* [2015] found that at longer timescales (~5 months) climate variability tends to have a larger impact on the background climate than soil moisture conditions. Our results show that the soil moisture conditions two weeks prior to a heatwave affects temperatures experienced during the first few heatwave days, with less conclusive results at longer periods of a month (not shown). It is likely that the timescales vary regionally and possibly according to the severity of the event. Therefore, while our results are consistent with existing research in Australia and Europe on the role of antecedent soil moisture conditions and heatwaves, further research is required to contrast regional differences and identify timescales.

5. Conclusions

In this study we diagnose the reasons why the land surface contribution to Australian heatwaves is not spatially homogeneous and link this to the model-derived estimates of land-atmosphere coupling. We demonstrate that in Northern Australia where the land-atmosphere coupling is strongly land-driven, heatwaves are hotter when there are drier soil moisture conditions two weeks prior to a heatwave event. Over South East Australia, dry antecedent soil moisture conditions are associated with warmer temperature anomalies on the first and second day of a heatwave event. For the drier southern parts of Australia, no discernible contribution of antecedent soil moisture conditions on temperature anomalies during a heatwave could be detected. Therefore, the impact of antecedent soil moisture conditions on heatwave intensity varies considerably across Australia. Furthermore, antecedent soil moisture conditions appear to have a greater impact than the daily evolution of the energy partitioning, particularly for heatwave intensity rather than the duration.

Characterizing the land surface according to different coupling regimes was critical to identifying the regions where the land surface may contribute to heatwave intensity. In this paper, we split regions into those where surface temperatures are sensitive to variations in sensible heating (land-driven coupling) and those where surface temperatures are decoupled from variations in local sensible heating (atmospheric-driven coupling). Over these atmospheric-driven regions, local antecedent soil moisture conditions had no influence on heatwave intensity or frequency and these are likely driven by a combination of warm air advection and adiabatic heating. Surprisingly, when heatwaves occur along the east coast of Australia, where there is atmospheric-driven coupling and lower background temperature, temperature anomalies are higher compared to more inland locations where the land-driven coupling is strong. Differences in the frequency of heatwave days between the coupling regimes were also found, where regions with strong land-driven coupling tended to have a higher frequency of heatwave days. Therefore, the two-legged coupling indices were useful for distinguishing regional-scale differences and could be extended to separate other atmospheric mechanisms.

The timescales at which antecedent soil moisture conditions impact heatwave intensity requires further investigation, as our spatial analysis suggests that these vary between regions under different synoptic conditions. Disentangling the local versus remote contributions to the accumulation of heat is a necessary step in future research investigating the role of both spatial and temporal heterogeneity of land surface contributions to heatwaves. Resolving these knowledge gaps is a necessary requirement before integrating land surface information into heatwave warning systems and understanding how heatwaves may evolve with climate change.

Acknowledgements

We are grateful to the ECMWF for using the ERA-Interim reanalysis as boundary conditions for all regional climate models presented in this study. We thank the NCAR Mesoscale and Microscale Meteorology Division for developing and maintaining the Weather Research and Forecasting Model. The computational modelling was supported by the National Computational Infrastructure (NCI) at the Australian National University in Canberra, Australia; the Pawsey Supercomputing Centre in Perth, Western Australia; and the German Climate Research Centre (DKRZ) infrastructure. This project is supported through funding from the Australian Research Council (ARC) Centre of Excellence for Climate Extremes (CE170100023). Sarah E. Perkins-Kirkpatrick is supported by an ARC Future Fellowship (FT170100106). Daniel Argüeso is funded by the European Union's Horizon 2020 programme through the Marie Skłodowska-Curie grant (H2020-MSCA-IF-2016-743547). Jatin Kala is supported by the ARC Discovery Early Career Research Grant (DE170100102). All CORDEX AustralAsia data is published on the Earth System Grid Federation. Data for the WRF simulations is available on the NCI ESGF node in the CORDEX Research Collection (https://esgf.nci.org.au/search/esgf-nci/). Data for the CCLM and CCAM simulations is available at the Lawrence Livermore National Laboratory ESGF node available at https://esgf-node.llnl.gov/search/esgf-llnl/. All software scripts to process the

data and reproduce the analysis are in the process of being archived at https://github.com/annettehirsch/hirsch-jgra-2019.git.

References

Andrys J., T. J. Lyons, and J. Kala [2015] Multidecadal evaluation of WRF downscaling capabilities over Western Australia in simulating rainfall and temperature extremes. J. Appl. Met. Climatol., 54, 370-394, doi:10.1175/JAMC-D-14-0212.1.

Argüeso D., J. P. Evans, A. J. Pitman, and A. Di Luca [2015] Effects of city expansion on heat stress under climate change conditions. PLoS ONE, 10, e0117066, doi:10.1371/journal.pone.0117066.

Bechtold P. et al. [2008] Advances in simulating atmospheric variability with the ECMWF model: From synoptic to decadal time-scales. Quart. J. Roy. Met. Soc., 134, 1337-1351, doi:10.1002/qj.289.

Cowan T., G. C. Hegerl, I. Colfescu, M. Bollasina, A. Purich, and G. Boschat [2017] Factors contributing to record-breaking heat waves over the Great Plains during the 1930s Dust Bowl. J. Climate, 30, 2437-2461, doi:10.1175/JCLI-D-16-0436.1.

Cowan T., A. Purich, S. Perkins, A. Pezza, G. Boschat, and K. Sadler [2014] More frequent, longer, and hotter heat waves for Australia in the twenty-first century. J. Clim., 27, 5851-5871, doi:10.1175/JCLI-D-14-00092.1.

Decker M., A. J. Pitman, and J. P. Evans [2015] Diagnosing the seasonal land–atmosphere correspondence over northern Australia: dependence on soil moisture state and correspondence strength definition. Hydrol. Earth. Syst. Sci., 19, 3433–3447, doi: 10.5194/hess-19-3433-2015

Decker M., M. A. Brunke, Z. Wang, K. Sakaguchi, X. Zeng, and M. G. Bosilovich [2012] Evaluation of reanalysis products from GSFC, NCEP, and ECMWF using flux tower observations. J. Clim., 25, 1916-1944, doi:10.1175/JCLI-D-11-00004.1.

Dee D.P., et al. [2011] The ERA-Interim reanalysis: configuration and performance of the data assimilation system. Quarterly Journal of the Royal Meteorological Society, 137(656):553-597. doi:10.1002/qj.828.

Di Luca A., D. Argüeso, J. P. Evans, R. de Elía, and R. Laprise [2016] Quantifying the overall added value of dynamical downscaling and the contribution from different spatial scales. J. Geophys. Res. Atmos., 121- 1575-1590, doi:10.1002/2015JD024009.

Di Virgilio G., J. P. Evans, A. Di Luca, R. Olson, D. Argüeso, J. Kala, J. Andrys, P. Hoffmann, J. Katzfey, and B. Rockel [2019] Evaluation of ERA-Interim-driven CORDEX regional climate model simulations over Australia. Clim. Dyn., 53, 2985, doi:10.1007/s00382-019-04672-w.

Dirmeyer P. A., et al. [2014] Intensified land surface control on boundary layer growth in a changing climate. Geophys. Res. Lett., 41, doi:10.1002/2013GL058826.

Dirmeyer P. A., Y. Jin, B. Singh and X. Yan [2013a] Evolving Land-Atmosphere Interactions over North America from CMIP5 Simulations. J. Clim., 26, 7313-7327, doi:10.1175/JCLI-D-12-00454.1.

Dirmeyer P. A., Y. Jin, B. Singh and X. Yan [2013b] Trends in Land-Atmosphere Interactions from CMIP5 Simulations. J. Hydrometeor., 14, 829-849, doi:10.1175/JHM-D-12-0107.1.

Dirmeyer, P. A., 2011: The terrestrial segment of soil moisture-climate coupling. Geophys. Res. Lett., 38, L16702, doi:10.1029/2011GL048268.

Donat M. G., A. J. Pitman, and S. I. Seneviratne [2017] Regional warming of hot extremes accelerated by surface energy fluxes. Geophys. Res. Lett., 44, doi:10.1002/2017GL073733.

Evans J. P., X. Meng, and M. F. McCabe [2017] Land surface albedo and vegetation feedbacks enhanced the millennium drought in south-east Australia. Hydrol. Earth Syst. Sci., 21, 409-422, 2017.

Evans J. P., F. Ji, C. Lee, P. Smith, D. Argüeso, and L. Fita [2014] Design of a regional climate modelling projection ensemble experiment - NARCliM. Geosci. Model Dev., 7, 621-629, doi:10.5194/gmd-7-621-2014.

Evans J. P., M. Ekström, and F. Ji [2012] Evaluating the performance of a WRF physics ensemble over South-East Australia. Clim. Dyn., 39, 1241-1258, doi:10.1007.s00382-011-1244-5.

Ferranti L. and P. Viterbo [2006] The European Summer of 2003: Sensitivity to soil water initial conditions. J. Climate, 19, 3659-3680, doi:10.1175/JCLI3810.1.

Fischer E.M., S. I. Seneviratne, D. Lüthi, and C. Schär [2007a] Contribution of land-atmosphere coupling to recent European summer heat waves. Geophys. Res. Lett., 34, L06707, doi:10.1029/2006GL029068.

Fischer E.M., S. I. Seneviratne, P. L. Vidale, D. Lüthi, and C. Schär [2007b] Soil Moisture–Atmosphere Interactions during the 2003 European Summer Heat Wave. J. Climate, 20, 5081–5099, doi:10.1175/JCLI4288.1.

Flach M., S. Sippel, F. Gans, A. Bastos, A. Brenning, M. Reichstein, and M. D. Machecha [2018] Contrasting biosphere responses to hydrometeorological extremes: revisiting the 2010 western Russian heatwave. Biogeosciences Discuss., doi:10.5194/bg-2018-130.

Ford T. W. and J. Schoof [2016] Oppressive heat events in Illinois related to antecedent wet soils. J. Hydrometeor., 17, 2713-2726, doi:10.1175/JHM-D-16-0075.1.

Gao Y., J. S. Fu, J. B. Drake, Y. Liu, and J.-F. Lamarque [2012] Projected changes of extreme weather events in the eastern Unitted States based on a high resolution climate modeling system. Environ. Res. Lett., 7, 04425 (12pp), doi:10.1088/1748-9326/7/4/044025.

Gibson P. B., A. J. Pitman, R. Lorenz, and S. E. Perkins-Kirkpatrick [2017] The role of circulation and land surface conditions in current and future Australian heat waves. J. Climate, 30, 9933-9948, doi:10.1175/JCLI-D-17-0265.1.

Giorgi F., C. Jones, and G. Asrar [2009] Addressing climate information needs at the regional level: The CORDEX framework. WMO Bulletin, 53,175-183.

Hauser, M., R. Orth, and S. I. Seneviratne [2016] Role of soil moisture versus recent climate change for the 2010 heatwave in western Russia. Geophys. Res. Lett., 43, 2819-2826, doi:10.1002/2016GL068036.

Herold N., M. Ekström, J. Kala, J. Goldie, and J. P. Evans [2018] Australian climate extremes in the 21st century according to a regional climate model ensemble: implications for health and agriculture. Weather. Clim. Extr., 20, 54-68, doi:10.1016/j.wace.2018.01.001.

Herold N., J. Kala, and L. V. Alexander [2016] The influence of soil moisture deficits on Australian heatwaves. Env. Res. Lett., 11, 064003, doi:10.1088/1748-9326/11/6/064003.

Hirsch A. L., A. J. Pitman, and V. Haverd [2016] Evaluating land-atmosphere coupling using a resistance pathway framework. J. Hydrometeorol., 17, 2615-2630, doi:10.1175/JHM-D-15-0204.1.

Hirsch A. L., A. J. Pitman, J. Kala, R. Lorenz, and M. G. Donat [2015] Modulation of land-use change impacts on temperature extremes via land-atmosphere coupling over Australia. Earth Int., 19, 012, doi:10.1175/EI-D-15-0011.1.

Hirsch A. L., A. J. Pitman, S. I. Seneviratne, J. P. Evans, and V. Haverd [2014] Summertime maximum and minimum temperature asymmetry over Australia determined using WRF. Geophys. Res. Lett., 41, 1546–1552, doi: 10.1002/2013GL059055.

Holgate, C. M., A. I. J. M. Van Dijk, J. P. Evans, and A. J. Pitman [2019] The importance of the one dimensional assumption in soil moisture - rainfall depth correlation at varying spatial scales. J. Geophys. Res. Atmos., doi:10.1029/2018JD029762.

Horton R. M., J. S. Mankin, C. Lesk, E. Coffel, and C. Raymond [2016] A review of recent advances in research on extreme heat events. Curr. Clim. Change Rep., 2, 242-259, doi:10.1007/s40641-016-0042-x.

Ji F., M. Ekström, J. P. Evans, and J. Teng [2014] Evaluating rainfall patterns using physics scheme ensembles from a regional atmospheric model. Theoret. Appl. Climatol., 115, 297-304, doi:10.1007/s00704-013-0904-2.

Jones D., W. Wang, and R. Fawcett [2009] High-quality spatial climate data-sets for Australia. Aust. Meteor. Mag., 58, 233–248.

Kala J., J. P. Evans, and A. J. Pitman [2015a] Influence of antecedent soil moisture conditions on the synoptic meteorology of the Black Saturday bushfire event in southeast Australia. Q. J. R. Meteorol. Soc., 141, 3118-3129, doi:10.1002/qj.2596.

Kala J., J. Andrys, T. J. Lyons, I. J. Foster, and B. J. Evans [2015b] Sensitivity of WRF to driving data and physics options on a seasonal time-scale for the southwest of Western Australia. Clim. Dyn., 44, 633-659, doi:10.1007/s00382-014-2160-2.

King A. D., L. V. Alexander, and M. G. Donat [2013] The efficacy of using gridded data to examine extreme rainfall characteristics: A case study for Australia. Int. J. Climatol., 33, 2376-2387, doi:10.1002/joc.3588.

Knist S. et al. [2017] Land-atmosphere coupling in EURO-CORDEX evaluation experiments. J. Geophys. Res. Atmos., 122, 79-103, doi:10.1002/2016JD025476.

Lewis, S. C. and A. D. King [2015] Dramatically increased rate of observed hot record breaking in recent Australian temperatures. Geophys. Res. Lett., 42, 7776-7784, doi:10.1002/2015GL065793.

Lewis, S. C. and D. J. Karoly [2013] Anthropogenic contributions to Australia's record summer temperatures of 2013. Geophys. Res. Lett., 40, 3705-3709, doi:10.1002/grl.50673.

Lorenz R., A. J. Pitman, A. L. Hirsch, and J. Srbinovsky [2015] Intraseasonal versus interannual measures of land-atmosphere coupling strength in a global climate model: GLACE-1 versus GLACE-CMIP5 experiments in ACCESS1.3b. J. Hydrometeorol., 16, 2276-2295, doi:10.1175/JHM-D-14-0206.1.

Lorenz R., E. B. Jaegar, and S. I. Seneviratne [2010] Persistence of heatwaves and its link to soil moisture memory. Geophys. Res. Lett., 37, L09703, doi:10.1029/2010GL042764.

McGregor J. L. and M. R. Dix [2008] An updated description of the Conformal-Cubic atmospheric model. High Resolution Numerical Modelling of the Atmosphere and Ocean. Springer, New York. doi:10.1007/978-0-387-49791-4_4.

Maraun D. et al. [2017] Towards process-informed bias correction of climate change simulations. Nature Clim. Change., 7, 764-773, doi:10.1038/NCLIMATE3418.

Martens B., et al. [2017] GLEAM v3: satellite-based land evaporation and root-zone soil moisture. Geoscientific Model Development, 10, 1903-1925. doi:10.5194/gmd-10-1903-2017.

Miralles D. G., A. J. Teuling, C. C. van Heerwaarden, and J. Vilá-Guerau de Arellano [2014] Mega-heatwave temperatures due to combined soil desiccation and atmospheric heat accumulation. Nature Geoscience, 7, 345-349, doi:10.1038/ngeo2141.

Miralles D.G., et al. [2011] Global land-surface evaporation estimated from satellite-based observations. Hydrology and Earth Systems Sciences, 15, 453-469. doi:10.5194/hess-15-453-2011.

Mueller B. and S. I. Seneviratne [2012] Hot days induced by precipitation deficits at the global scale. Proc. Nat. Aca. Sci., 109, 12398-12403, doi:10.1073/pnas.1204330109.

Nairn J. and R. Fawcett [2013] Defining heatwaves: heatwaves defined as a heat impact event servicing all community and business sectors in Australia. CAWCR Technical report No 060. The Centre for Australian Weather and Climate Research A partnership between the Bureau of Meteorology and CSIRO.

Nicolai-Shaw N, J. Zscheischler, M. Hirschi, L. Gudmundsson, and S. I. Seneviratne [2017] A drought event composite analysis using satellite remote-sensing based soil moisture. Remote Sens. Env., 203, 216-225, doi:10.1016/j.rse.2017.06.014.

Parker T. J., G. J. Berry, and M. J. Reeder [2014a] The structure and evolution of heat waves in Southeastern Australia. J. Clim., 27, 5768-5785, doi:10.1175/JCCLI-D-13-00740.1.

Parker T. J., G. J. Berry, M. J. Reeder, and N. Nicholls [2014b] Modes of climate variability and heat waves in Victoria, southeastern Australia. Geophys. Res. Lett., 41, 6926-6934, doi:10.1002/2014GL061736.

Perkins S. E. [2015] A review on the scientific understanding of heatwaves - their measurement, driving mechanisms, and changes at the global scale. Atmos. Res., 164-165, 242-267, doi:10.1016/j.atmosres.2015.05.014.

Perkins S. E., D. Argüeso, and C. J. White [2015] Relationships between climate variability, soil moisture, and Australian heatwaves. J. Geophys. Res. Atmos., 120, 8144-8164, doi:10.1002/2015JD023592.

Perkins S.E. and P. B. Gibson [2015] Increased risk of the 2014 Australian May heatwave due to anthropogenic activity [in “Explaining Extremes of 2014 from a Climate Perspective”]. Bull. Am. Meteorol. Soc., 96, S154-S157, doi:10.1175/BAMS-D-15-00074.1.

Perkins S.E., S. L. Lewis, A. D. King, and L. V. Alexander [2014a] Increase simulated risk of the hot Australian summer of 2012/2013 due to anthropogenic activity as measured by heat wave frequency and intensity [in “Explaining Extremes of 2013 from a Climate Perspective”]. Bull. Am. Meteorol. Soc. 95 (9), S34–S36.

Perkins S. E., A. Moise, P. Whetton, and J. Katzfey [2014b] Regional changes of climate extremes over Australia—a comparison of regional dynamical downscaling and global climate model simulations. Int. J. Climatol. 34, 3456–3478, doi:10.1002/joc.3927.

Perkins S. E. and L. V. Alexander [2013] On the measurement of heat waves. J. Clim., 26, 4500-4517, doi:10.1175/JCLI-D-12-00383.1.

Perkins S. E. and E. M. Fischer [2013] The usefulness of different realizations for the model evaluation of regional trends in heat waves. Geophys. Res. Lett., 40, 1-5, doi:10.1002/2013GL057833.

Quinting J. F., T. J. Parker, and M. J. Reeder [2018] Two synoptic routes to subtropical heatwaves as illustrated in the Brisbane region of Australia. Geophys. Res. Lett., 45, 10700-10708, doi:10.1029/2018GL079261.

Reichle R.H., et al. [2017] Assessment of MERRA-2 Land Surface Hydrology Estimates. Journal of Climate, 30(8):2937-2960. doi:10.1175/JCLI-D-16-0720.1.

Risbey J. S., T. J. O'Kane, D. P. Monselesan, C. L. E. Franzke, and I. Horenko [2018] On the dynamics of Austral heat waves. J. Geophys. Res. Atmos., 123, 38-57 doi:10.1002/2017JD027222.

Ritter B., and J.-F. Geleyn [1992] A comprehensive radiation scheme for numerical weather prediction models with potential applications in climate simulations. Mon. Wea. Rev., 120, 303-325, doi:10.1175/1520-0493(1992)120<0303:acrsfn>2.0.co;2.

Rockel B., A. Will, and A. Hense [2008] The Regional Climate Model COSMO-CLM (CCLM). Meteorol Z., 17, 347-348, doi:10.1127/0941-2948/2008/0309.

Salathé Jr. E. P., L. R. Leung, Y. Qian, and Y. Zhang [2010] Regional climate model projections for the State of Washington. Clim. Dyn., 102: 51-75, doi:10.1007/s10584-010-9849-y.

Santanello, J. A., P. A. Dirmeyer, C. R. Ferguson, K. L. Findell, A. B. Tawfik, A. Berg, M. Ek, P. Gentine, B. P. Guillod, C. van Heerwaarden, J. Roundy, and V. Wulfmeyer [2018] Land-Atmosphere Interactions: The LoCo Perspective. Bull. Amer. Meteor. Soc., 99, 1253-1272, doi:10.1175/BAMS-D-17-0001.1.

Seneviratne S. I., et al. [2013] Impact of soil moisture-climate feedbacks on CMIP5 projections: First results from the GLACE-CMIP5 experiment. Geophys. Res. Lett., 40, 5212-5217, doi: 10.1002/grl.50956.

Seneviratne S. I., et al. [2010] Investigating soil moisture–climate interactions in a changing climate: A review. Earth Sci. Rev., 99, 125–161, doi:10.1016/j.earscirev.2010.02.004.

Skamarock W. C., et al. [2008] A description of the Advanced Research WRF Version 3. NCAR Tech Note NCAR/TN-475+STR. NCAR. Boulder, CO.

Stott P. A., D. A. Stone, and M. R. Allen [2004] Human contribution to the European heatwave of 2003. Nature, 432, 610-614, doi:10.1038/nature03089.

Teng H., G. Branstator, G. A. Meehl, and W. M. Washington [2016] Projected intensification of subseasonal temperature variability and heat waves in the Great Plains. Geophys. Res. Lett., 43, 2165-2173, doi:10.1002/2015GL067574.

van der Linden E. C., R. J. Haarsma, and G. van der Schrier [2019] Impact of climate model resolution on soil moisture projections in central-western Europe. Hydrol. Earth Syst. Sci., 23, 191-206, doi:10.5194/hess-23-191-2019.

Vogel M. M., et al. [2017] Regional amplification of projected changes in extreme temperatures strongly controlled by soil moisture-temperature feedbacks. Geophys. Res. Lett., 44, 1511-1519, doi:10.1002/2016GL071235.

Tables with Captions

Table 1: CORDEX RCMs analysed in this paper over the period 1981 to 2010 for the AUS-44 domain using ERA-Interim as the boundary conditions.

Model (label)	Version	Land surface scheme	PBL scheme	Cumulus scheme	Radiation scheme
WRF (J)	3.6.0	Noah	Mellor-Yamada-Janjic	Kain-Fritsch	Dudhia/RRTM
WRF (K)	3.6.0	Noah	Mellor-Yamada-Janjic	Betts-Miller-Janjic	Dudhia/RRTM
WRF (L)	3.6.0	Noah	Yonsei University	Kain-Fritsch	CAM3
WRF (M)	3.3.0	Noah	Yonsei University	Kain-Fritsch	Dudhia/RRTM
CCLM	4.8.17-CLM3-5	CLM3.5	Prognostic turbulent kinetic	*Bechtold et al.* [2008]	*Ritter and Geleyn* [1992]

			energy		
CCAM		CABLEv2.2.3	Monin-Obukhov Similarity Theory	Mass Flux Closure	GFDL

Table 2: Datasets used in the model validation.

Name	Key reference	Native resolution	Variables (CF convention)
AGCD	*Jones et al.* [2009]	0.05˚ lat. x 0.05˚ lon.	tasmax, tasmin, pr
GLEAMv3.2a	*Martens et al.* [2017]; *Miralles et al.* [2011]	0.25˚ lat. x 0.25˚ lon.	hfls
MERRA2	*Reichle et al.* [2017]	0.5˚ lat. x 0.625˚ lon.	albedo, hfls, hfss, rlds, rlus, rsds, rsus, tas, ts, pr
ERAINT	*Dee et al.* [2011]	0.75˚ lat. x 0.75˚ lon.	hfls, hfss, rsds, rlds, tas, ts, pr

Table 3: EHF Heatwave Diagnostics

Acronym	Attribute	Description	Units
HWAt	Amplitude	Temperature anomaly above T_{90} for the hottest event per year	˚C
HWMt	Amplitude	Mean temperature anomaly above T_{90} for all events per year	˚C
HWF	Frequency	Percentage of days per year that are classified a heatwave day	% days
HWN	Frequency	Number of events per year	#/Year
HWD	Duration	Duration of the longest heatwave per year	days
WDL	Duration	Mean duration of all events per year	days

Figure Captions

Figure 1: CORDEX AustralAsia domain including topographic height [m] and regional analysis domains including: Northern Australia (NA), Eastern Australia (EA), South-East Australia (SEA), South Australia (SA), Nullarbor Plain (NP) and South-Western Australia (SWA). Note that the Great Dividing Range is the region with high topography along the East coast of Australia.

Figure 2: November to March climatological mean over 1981 to 2009 for the 2m air temperature 90th percentile. (a) AGCD; (b) MERRA2 minus AGCD; (c) ERAINT minus AGCD; (d) WRFJ minus AGCD; (e) WRFK minus AGCD; (f) WRFL minus AGCD; (g) WRFM minus AGCD; (h) CCLM minus AGCD and (i) CCAM minus AGCD. All panels are in units of ˚C. Values within ±0.1˚C or the observational uncertainty (b - i) are masked in white.

Figure 3: Relative model skill summary for all heatwave diagnostics defined in Table 3. The left panel shows the observational uncertainty characterised by the 10th to 90th percentile range of the difference between AGCD, MERRA2 and ERAINT. The right panel shows how much the model bias exceeds the observational uncertainty with blue indicating a negative bias in the 10th percentile, red indicating a positive bias in the 90th percentile, and white indicating that either the 10th or 90th percentile of the model bias is within the observational uncertainty. All biases are calculated using the heatwave diagnostics over the full period (1981-2009) and are expressed in relative terms [%].

Figure 4: Average anomaly time series relative to the calendar day 1981-2009 mean of surface climate variables from 30 days pre-heatwave to 14 days post-heatwave. Aggregating for all events over 1981-2009 and all land grid cells within the regions defined in Figure 1. The columns correspond to three regions depicted in Figure 1: Northern Australia (NA), South-East Australia (SEA), and the Nullarbor Plain (NP). The rows correspond to the variables: 2m air temperature (tas; ˚C), precipitation (pr; mm day^{-1}), soil moisture (mrso; kg m^{-2}), and the latent heat flux (hfls, W m^{-2}). For AGCD/GLEAM (yellow), MERRA2 (black), ERAINT (grey), WRFJ (blue), WRFK (red), WRFL (green), WRFM (purple), CCLM (cyan), and CCAM (magenta). AGCD is only available for tas and pr and GLEAM is only available for hfls. The start of the heatwave is marked by the vertical dashed lines.

Figure 5: Probability of a negative trend in the latent heat flux (hfls) for the 14 days prior to a heatwave event. For AGCD/GLEAM (a), MERRA2 (b), ERAINT (c), WRFJ (d), WRFK (e), WRFL (f), WRFM (g), CCLM (h), and CCAM (i). Values less than 0.5 have been masked in white.

Figure 6: Kernel density function of the 14-day pre-heatwave trend in the latent heat flux (hfls) anomaly time series (W m^{-2} d^{-1}). Constructed from the regional timeseries of all heatwave events identified over 1981-2009. The hfls trends have been split according to the soil moisture state: driest quarter (Q1: solid line), middle 50% (Q1-Q3: dashed line), and the wettest quarter (Q3: dotted line). Distributions are constructed using all model data (individual models are provided in the supplementary) using all land grid cells defined with the sub-regions: Northern Australia (a), Eastern Australia (b), South East Australia (c), South Australia (d), Nullarbor Plain (e), and South West Australia (f). The p-value derived from a two sample Kolmogorov-Smirnov test between Q1 and Q3 is included.

Figure 7: As in Figure 6 but for the 2m air temperature on the first day of the heatwave.

Figure 8: Kernel density function of the 2m air temperature on the first day of the heatwave. Constructed from the regional timeseries of all heatwave events identified over 1981-2009. The 2m air temperature have been split according to the sign of the 14-day pre-heatwave trend in the latent heat flux (hfls) anomaly time series: decreasing trend (solid line), and increasing (dashed line). Distributions are constructed using all model data using all land grid cells defined with the sub-regions: Northern Australia (a), Eastern Australia (b), South East Australia (c), South Australia (d), Nullarbor Plain (e), and South West Australia (f). The p-value derived from a two sample Kolmogorov-Smirnov test between the two distributions.

Figure 9: Normalized atmospheric coupling index (I_A) estimated for each model: WRFJ (a), WRFK (b), WRFL (c), WRFM (d), CCLM (e), and CCAM (f). Note that I_A is calculated for each heatwave season Oct-Mar over the period 1981-2009 and then normalized to enable comparison to the other coupling metrics. Values within ±0.05 are masked in white.

Figure 10: Kernel density function of the EHF_{SIG} heatwave diagnostics split between heatwave season grid cells with land-driven coupling (I_A > 0.1; red) and atmospheric-driven coupling (I_A < -0.1; blue). For each EHF diagnostic: Temperature anomaly for the hottest event (HWAt; ˚C; a), duration of the longest event (HWD; days; b), frequency of heatwave days (HWF; % days; c), mean temperature anomaly (HWMt; ˚C; d), mean duration (HWL; days; e), and number of events (HWN; #/Year; f). The vertical line denotes the likelihood ratio between land-driven coupling and tmospheric-driven coupling regimes exceeding the 90th percentile of the EHF_{SIG} metric with this threshold determined from the entire dataset.

Figure 11: As in Figure 10 but split according to the regions: Eastern Australia (EA; a and e), South-East Australia (SEA; b and f), South Australia (SA; c and g) and South-Western Australia (SWA; d and h). For (a-d) mean heatwave temperature anomaly above T_{90} (HWMt; ˚C) and (e-h) the percentage of heatwave days (HWF; % days). The vertical line denotes the likelihood ratio

between land-driven and atmospheric-driven coupling regimes exceeding the 90th percentile of the EHF_{SIG} metric with this threshold determined from the entire dataset. Northern Australia and the Nullarbor Plain sub-regions are omitted as these regions are predominantly only under one coupling regime.

Figure 12: Individual model likelihood ratios (LR) between the land-driven ($I_A > 0.1$) and atmospheric-driven ($I_A < -0.1$) regimes for temperature anomaly of hottest events (HWAt; ˚C; a), duration of longest events (HWD; days; b), percentage of heatwave days (HWF; % days; c), mean temperature anomaly (HWMt; ˚C; d), mean duration (HWL; days; e), and number of events (HWN; #/Year; f) evaluated according to the probability of exceeding the 90th percentile of each diagnostic. Note that the threshold is determined using all grid cells but probabilities are calculated according to the respective distribution of land-driven and atmospheric-driven coupling regions to account for differences in sample size.

Figure 1.

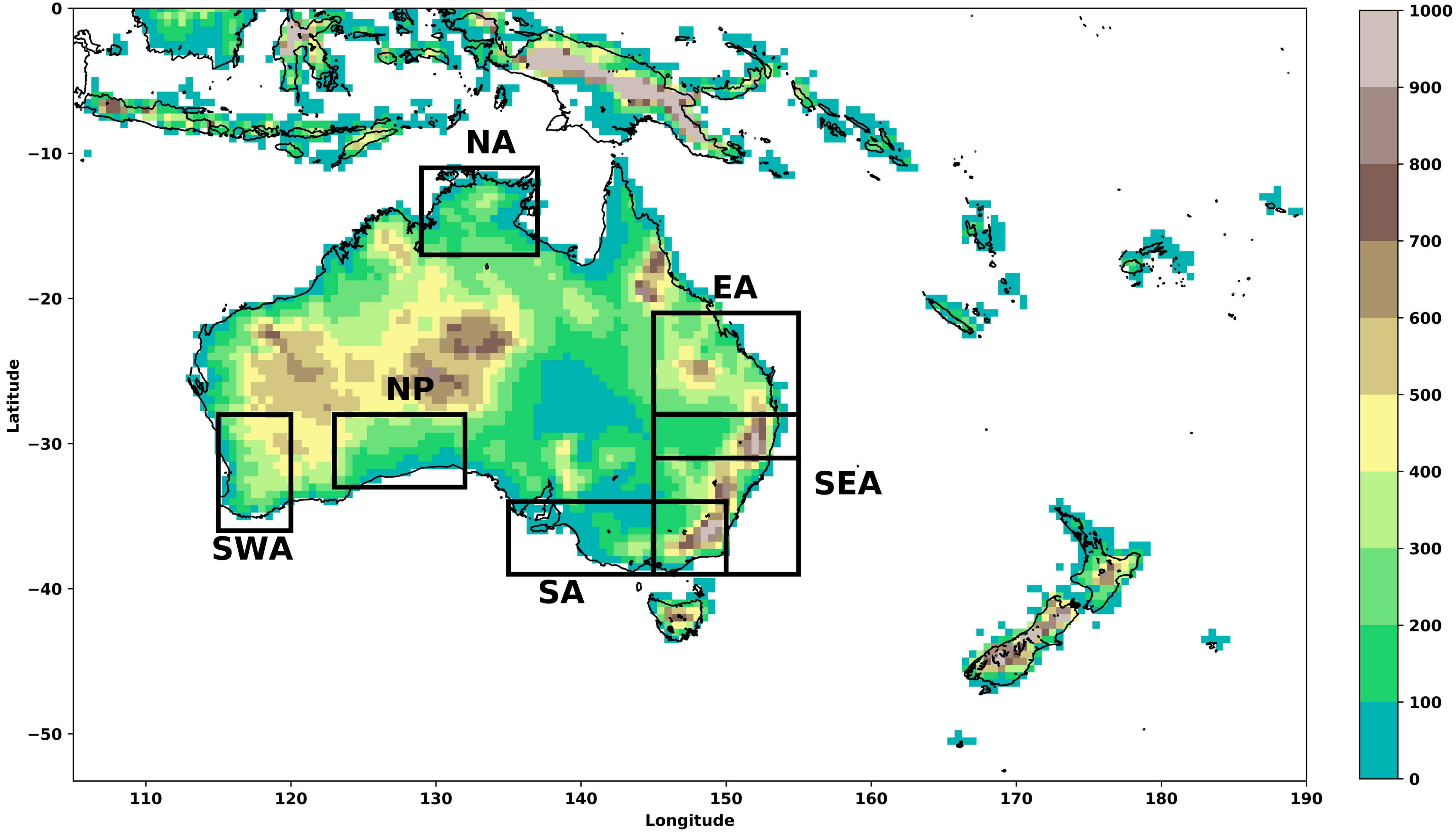

NA
EA
NP
SEA
SWA
SA
Latitude
Longitude
0
−10
−20
−30
−40
−50
110
120
130
140
150
160
170
180
190
1000
900
800
700
600
500
400
300
200
100
0

Figure 2.

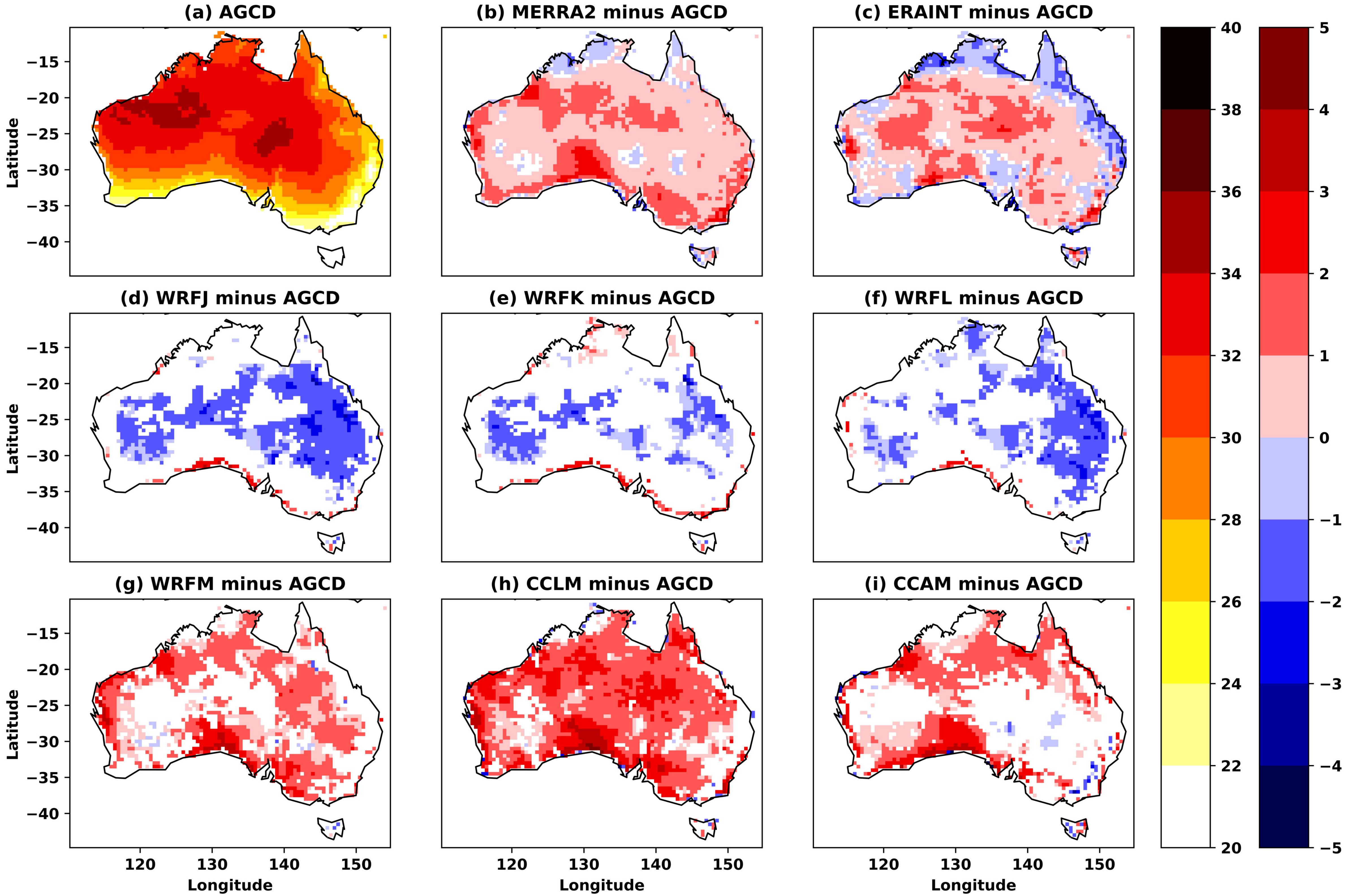

(a) AGCD
(b) MERRA2 minus AGCD
(c) ERAINT minus AGCD
(d) WRFJ minus AGCD
(e) WRFK minus AGCD
(f) WRFL minus AGCD
(g) WRFM minus AGCD
(h) CCLM minus AGCD
(i) CCAM minus AGCD
Latitude
Longitude
−15
−20
−25
−30
−35
−40
120
130
140
150
20
22
24
26
28
30
32
34
36
38
40
−5
−4
−3
−2
−1
0
1
2
3
4
5

Figure 3.

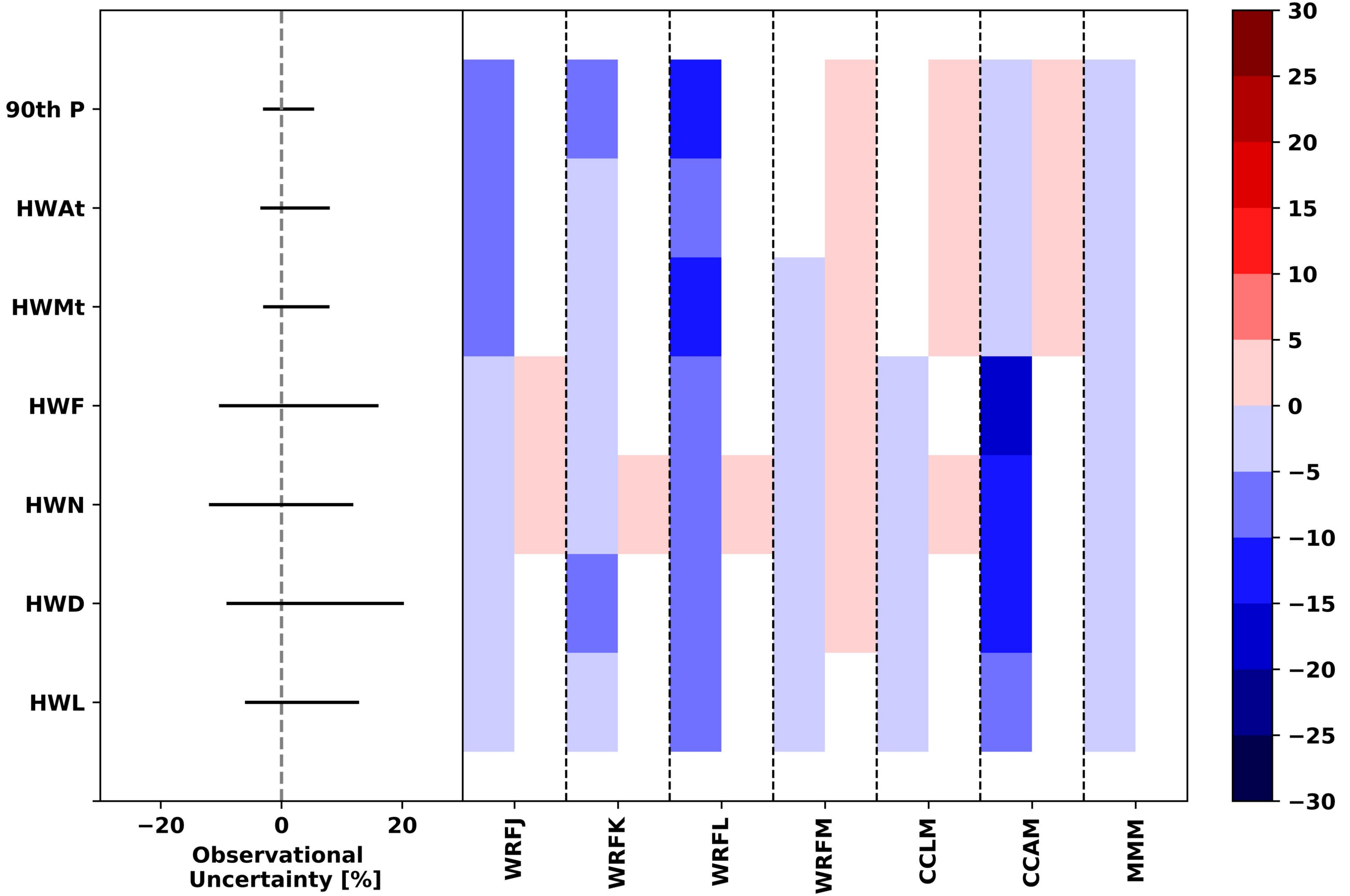
90th P
HWAt
HWMt
HWF
HWN
HWD
HWL
−20
0
20
Observational Uncertainty [%]
WRFJ
WRFK
WRFL
WRFM
CCLM
CCAM
MMM
30
25
20
15
10
5
0
−5
−10
−15
−20
−25
−30

Figure 4.

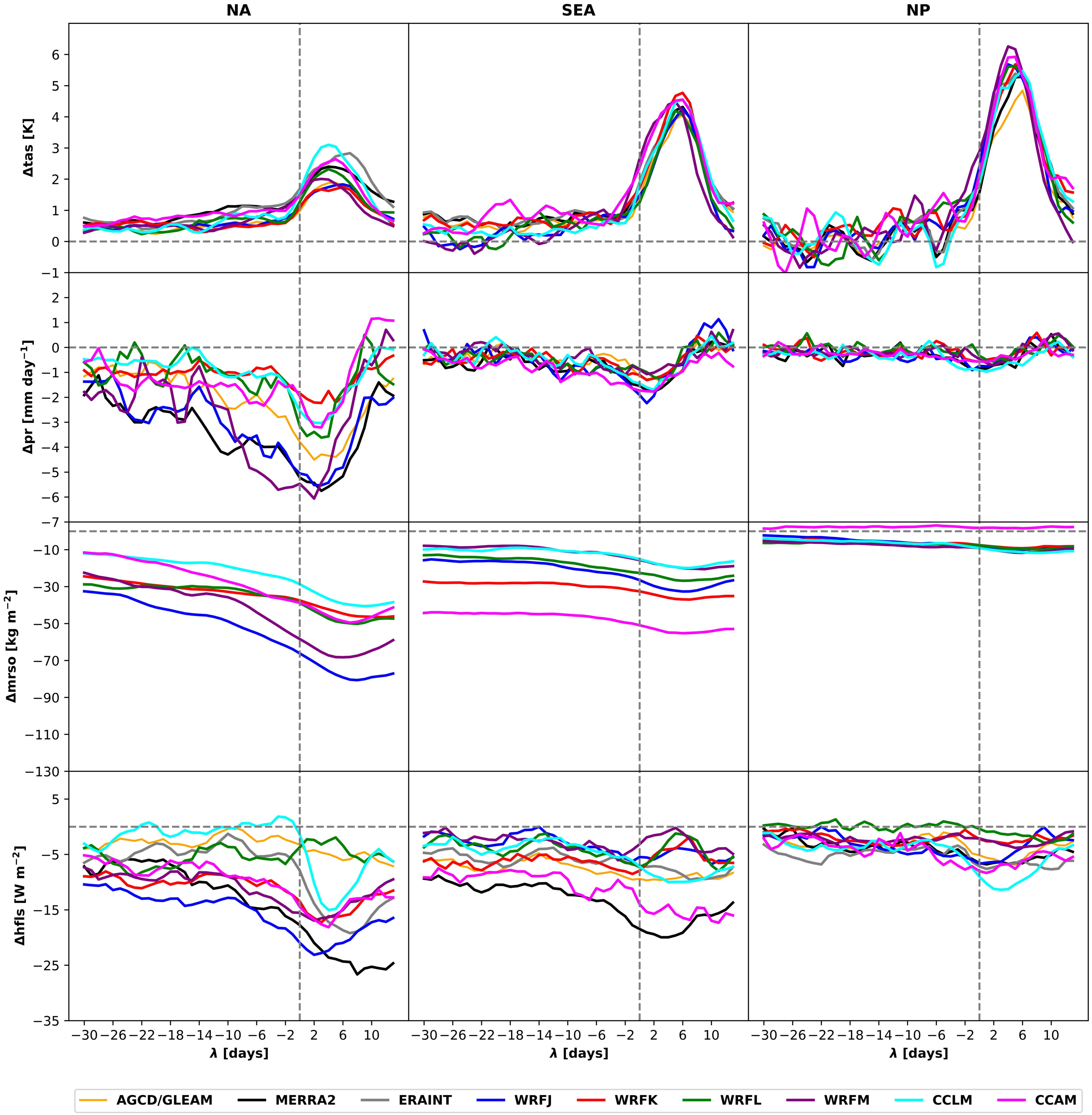
NA
SEA
NP
Δtas [K]
Δpr [mm day⁻¹]
Δmrso [kg m⁻²]
Δhfls [W m⁻²]
λ [days]
λ [days]
λ [days]
AGCD/GLEAM
MERRA2
ERAINT
WRFJ
WRFK
WRFL
WRFM
CCLM
CCAM

Figure 5.

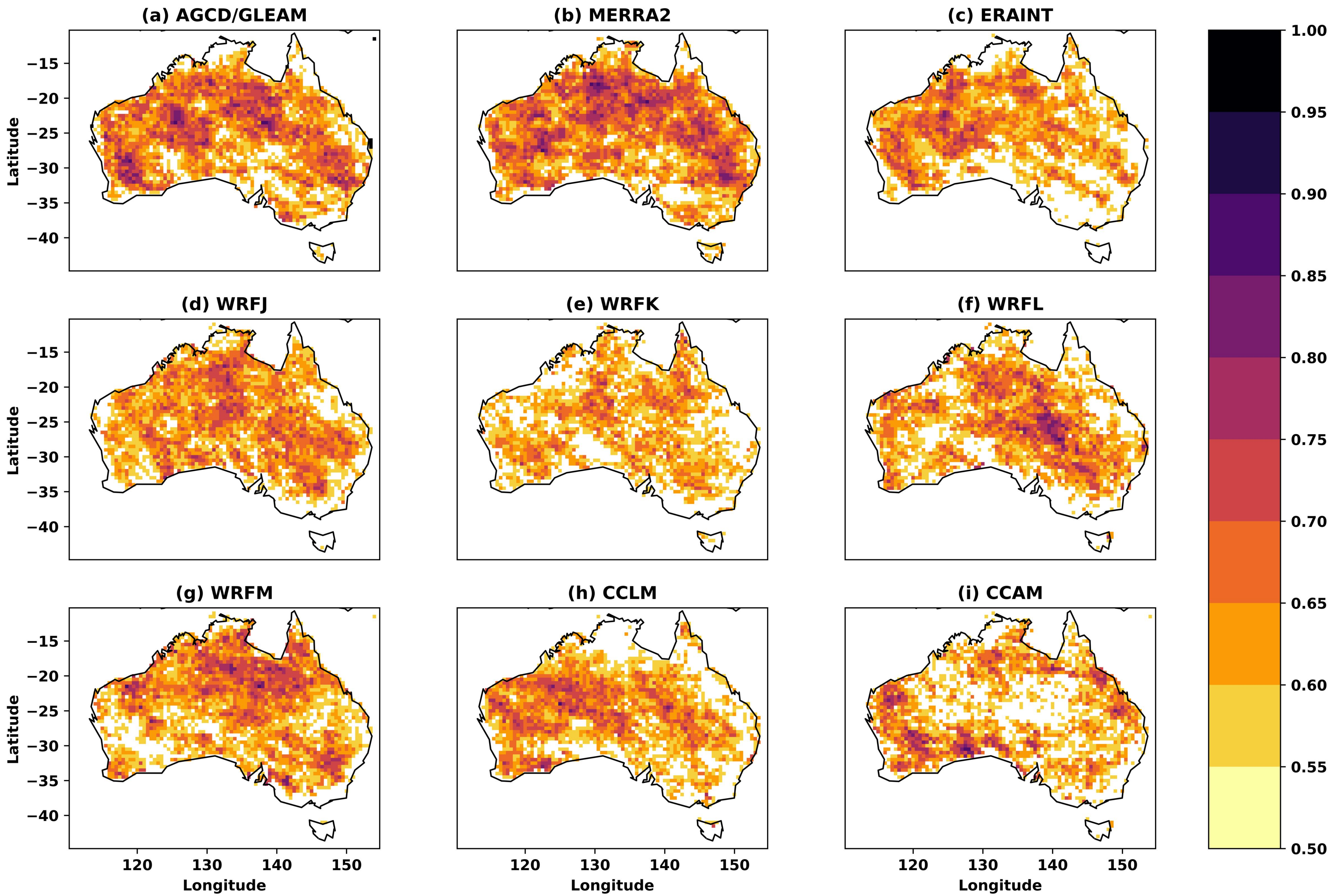

(a) AGCD/GLEAM
(b) MERRA2
(c) ERAINT
(d) WRFJ
(e) WRFK
(f) WRFL
(g) WRFM
(h) CCLM
(i) CCAM
Latitude
Longitude
−15
−20
−25
−30
−35
−40
120
130
140
150
1.00
0.95
0.90
0.85
0.80
0.75
0.70
0.65
0.60
0.55
0.50

Figure 6.

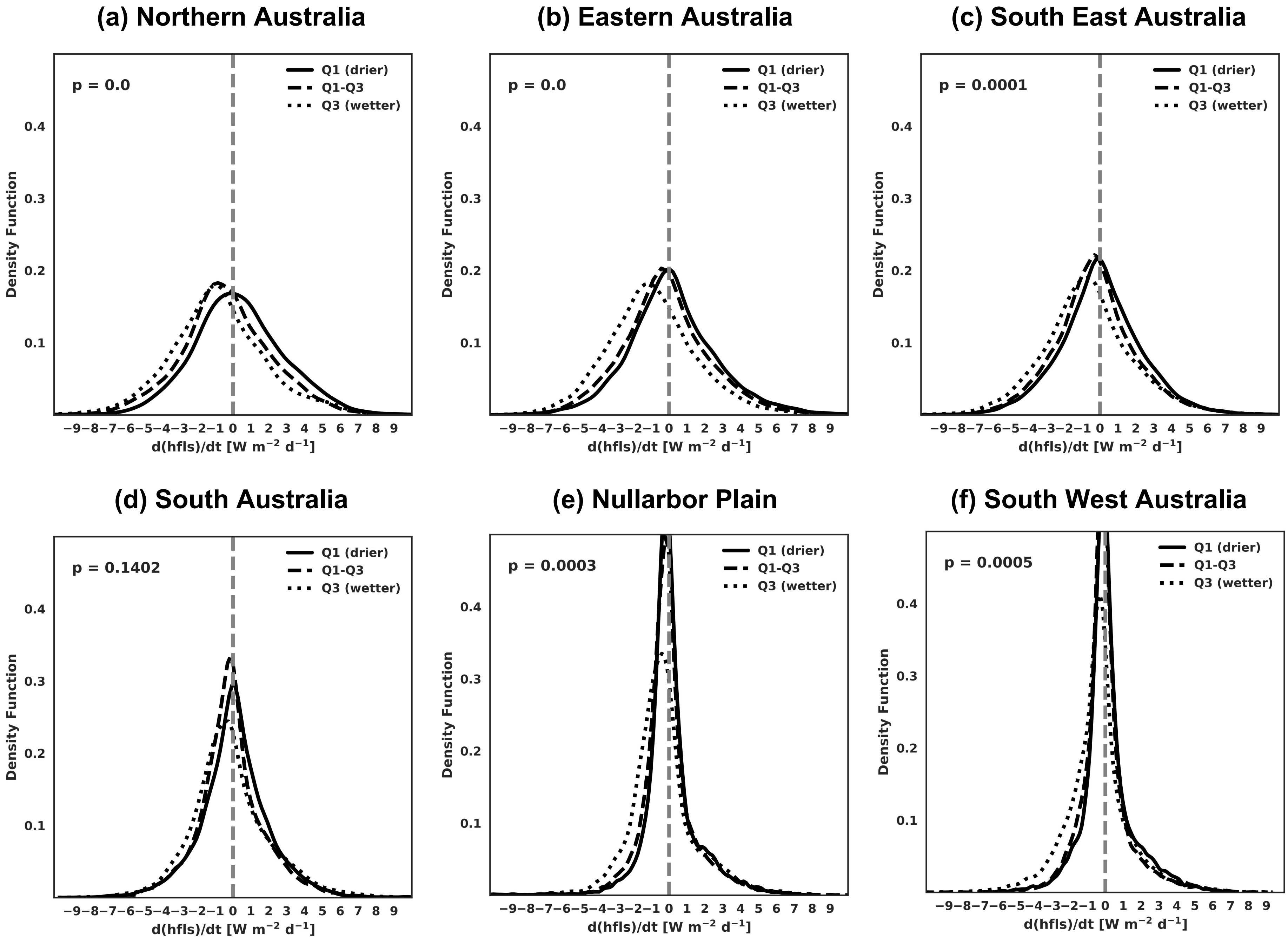
(a) Northern Australia
p = 0.0
(b) Eastern Australia
p = 0.0
(c) South East Australia
p = 0.0001
(d) South Australia
p = 0.1402
(e) Nullarbor Plain
p = 0.0003
(f) South West Australia
p = 0.0005
Q1 (drier)
Q1-Q3
Q3 (wetter)
Density Function
d(hfls)/dt [W m^{-2} d^{-1}]

Figure 7.

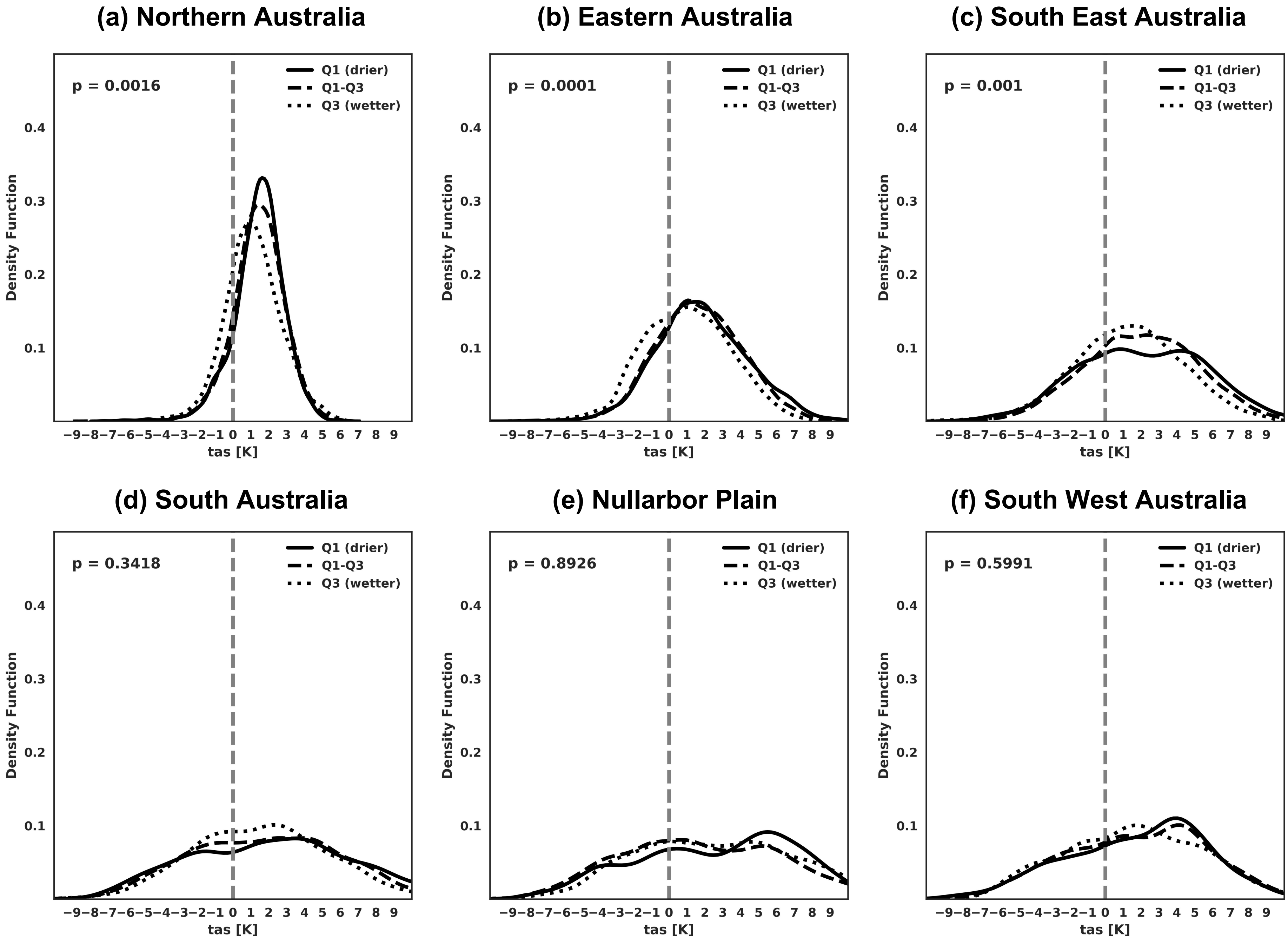
(a) Northern Australia
p = 0.0016
(b) Eastern Australia
p = 0.0001
(c) South East Australia
p = 0.001
(d) South Australia
p = 0.3418
(e) Nullarbor Plain
p = 0.8926
(f) South West Australia
p = 0.5991
Q1 (drier)
Q1-Q3
Q3 (wetter)
Density Function
tas [K]

Figure 8.

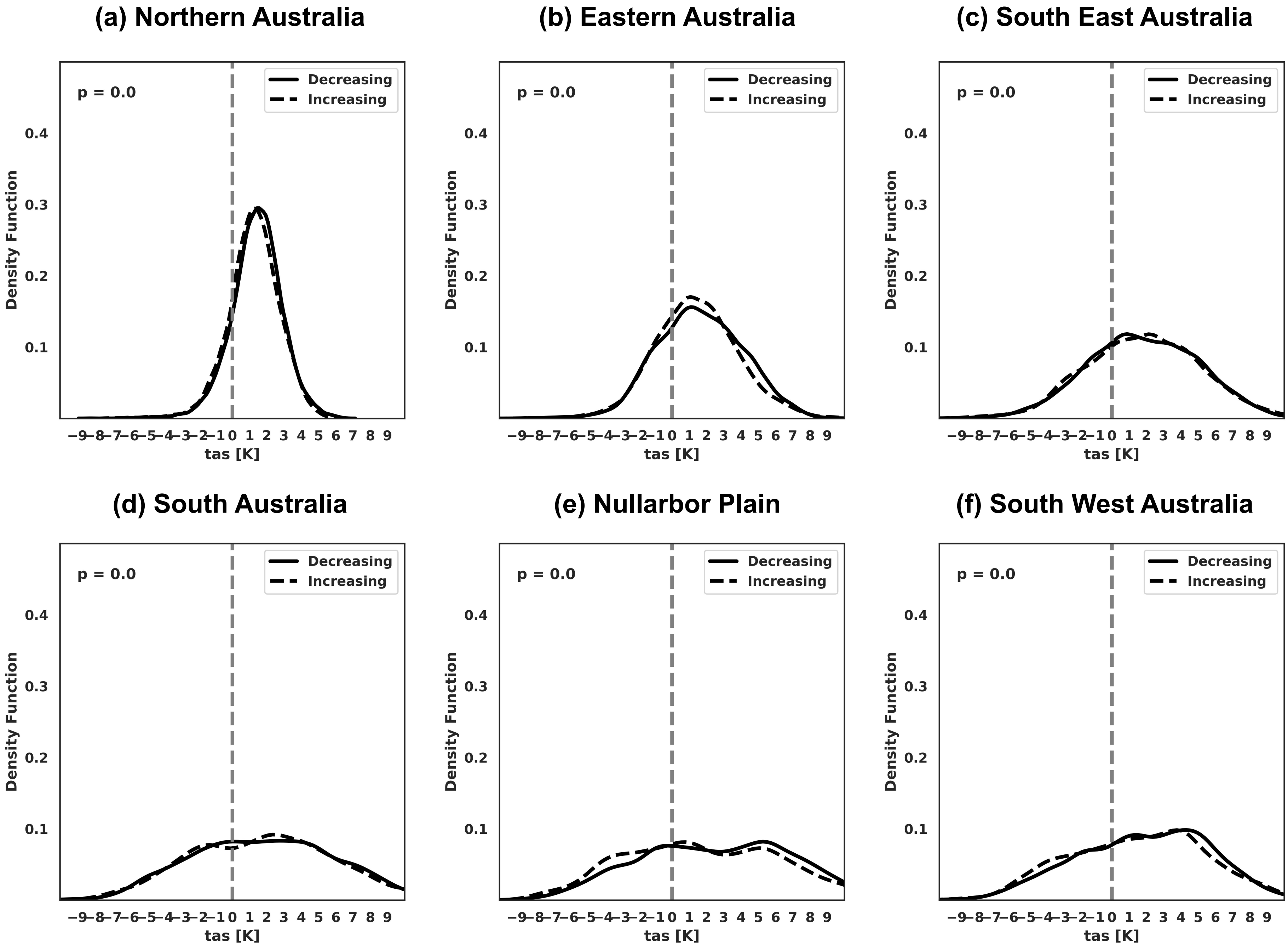
(a) Northern Australia
(b) Eastern Australia
(c) South East Australia
(d) South Australia
(e) Nullarbor Plain
(f) South West Australia
p = 0.0
Decreasing
Increasing
Density Function
tas [K]
0.1
0.2
0.3
0.4
−9 −8 −7 −6 −5 −4 −3 −2 −1 0 1 2 3 4 5 6 7 8 9

Figure 9.

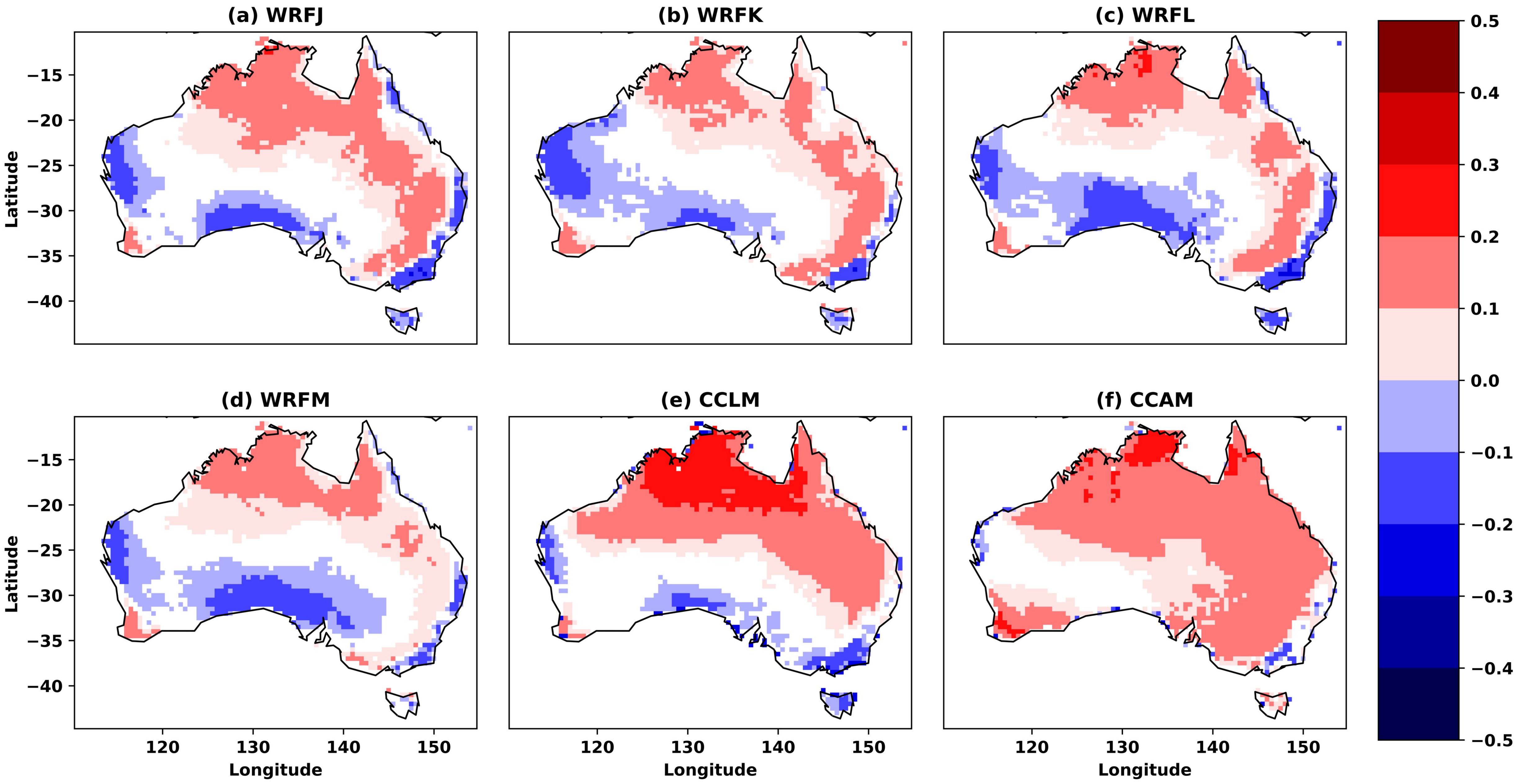

(a) WRFJ
(b) WRFK
(c) WRFL
(d) WRFM
(e) CCLM
(f) CCAM
Latitude
Longitude
−15
−20
−25
−30
−35
−40
120
130
140
150
0.5
0.4
0.3
0.2
0.1
0.0
−0.1
−0.2
−0.3
−0.4
−0.5

Figure 10.

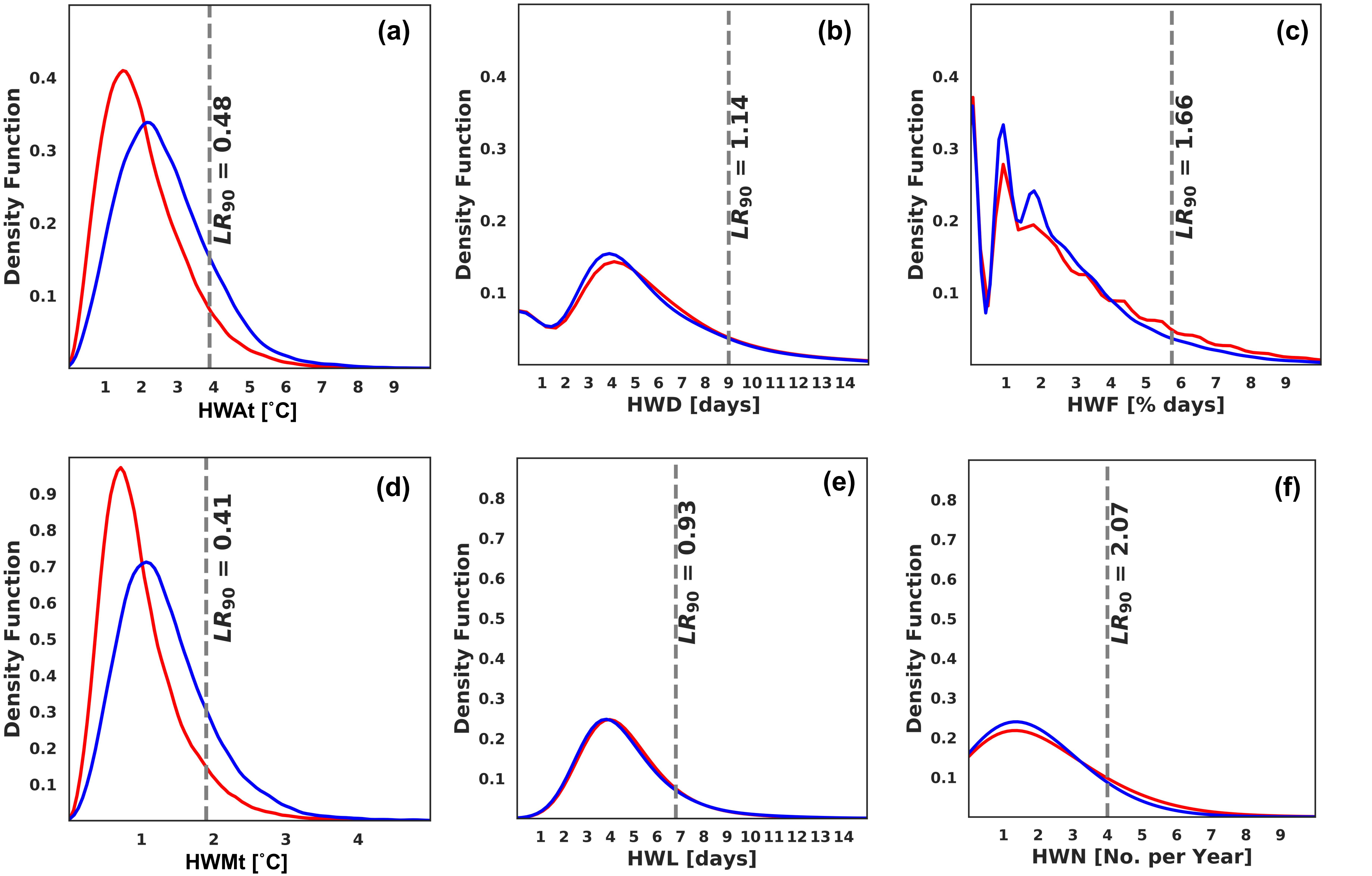
(a)
Density Function
HWAt [˚C]
LR_{90} = 0.48
(b)
Density Function
HWD [days]
LR_{90} = 1.14
(c)
Density Function
HWF [% days]
LR_{90} = 1.66
(d)
Density Function
HWMt [˚C]
LR_{90} = 0.41
(e)
Density Function
HWL [days]
LR_{90} = 0.93
(f)
Density Function
HWN [No. per Year]
LR_{90} = 2.07

Figure 11.

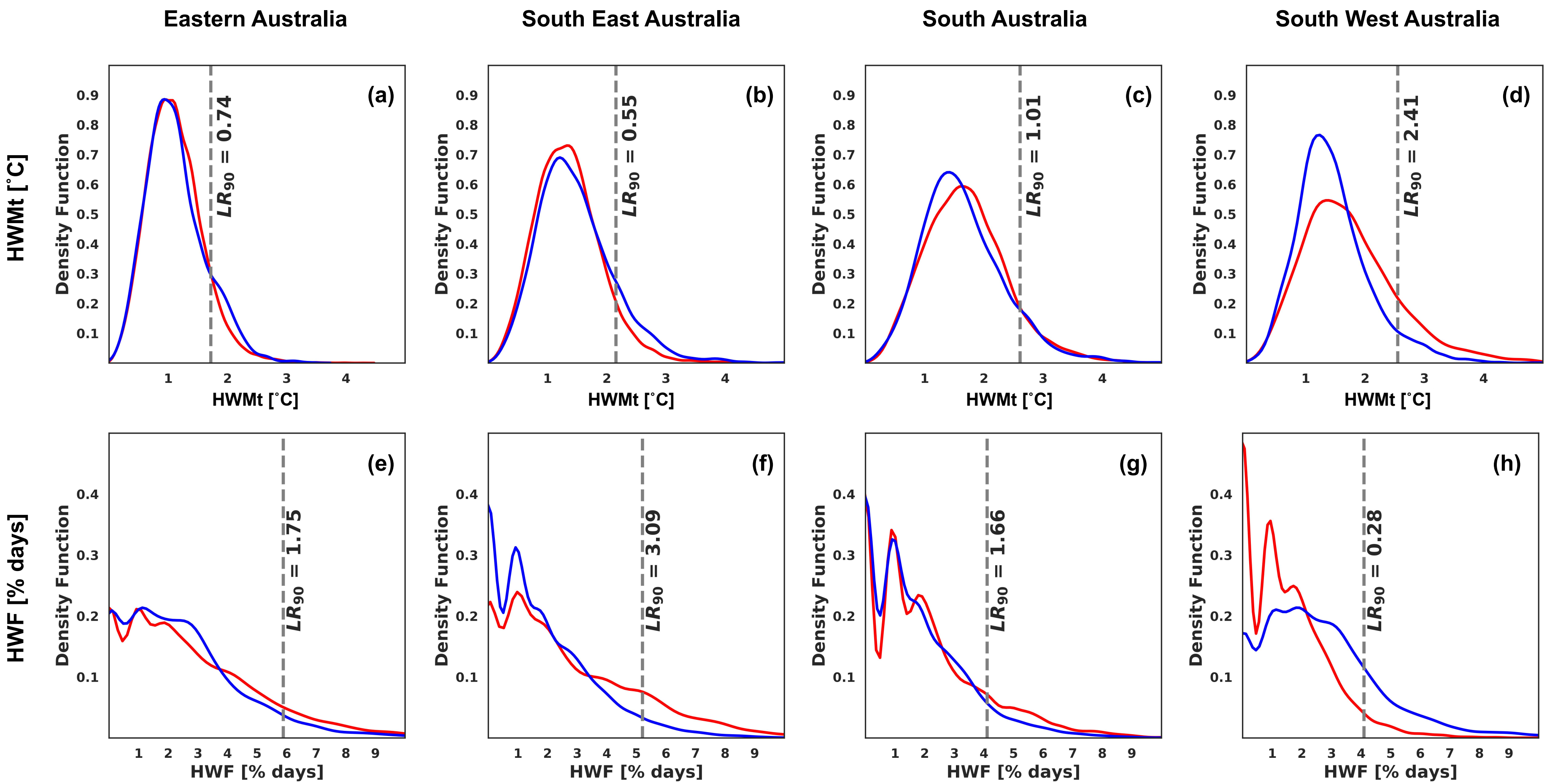

Eastern Australia
South East Australia
South Australia
South West Australia
HWMt [˚C]
HWF [% days]
Density Function
HWMt [˚C]
HWF [% days]
(a)
(b)
(c)
(d)
(e)
(f)
(g)
(h)
LR_{90} = 0.74
LR_{90} = 0.55
LR_{90} = 1.01
LR_{90} = 2.41
LR_{90} = 1.75
LR_{90} = 3.09
LR_{90} = 1.66
LR_{90} = 0.28

Figure 12.

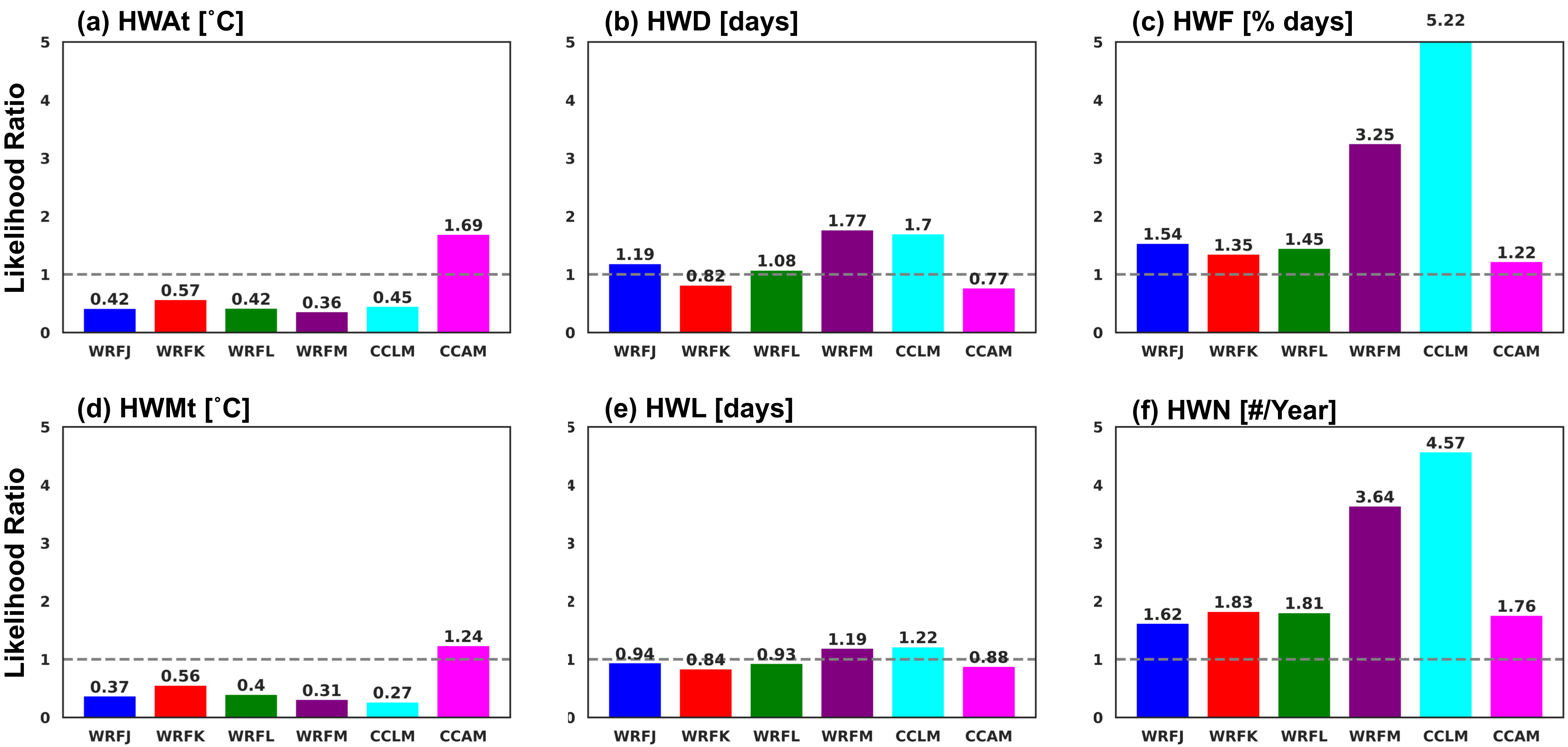
(a) HWAt [˚C]
(b) HWD [days]
(c) HWF [% days]
(d) HWMt [˚C]
(e) HWL [days]
(f) HWN [#/Year]
Likelihood Ratio
Likelihood Ratio
0
1
2
3
4
5
WRFJ
WRFK
WRFL
WRFM
CCLM
CCAM
0.42
0.57
0.42
0.36
0.45
1.69
1.19
0.82
1.08
1.77
1.7
0.77
1.54
1.35
1.45
3.25
5.22
1.22
0.37
0.56
0.4
0.31
0.27
1.24
0.94
0.84
0.93
1.19
1.22
0.88
1.62
1.83
1.81
3.64
4.57
1.76